



ELSEVIER

Contents lists available at ScienceDirect

Nuclear Instruments and Methods in  
Physics Research Ajournal homepage: [www.elsevier.com/locate/nima](http://www.elsevier.com/locate/nima)

## The PHENIX Forward Silicon Vertex Detector



C. Aidala<sup>j,1</sup>, L. Anaya<sup>k</sup>, E. Anderssen<sup>i</sup>, A. Bambaugh<sup>f</sup>, A. Barron<sup>k</sup>, J.G. Boissevain<sup>j</sup>, J. Bok<sup>l,k</sup>, S. Boose<sup>a</sup>, M.L. Brooks<sup>j,\*</sup>, S. Butsyk<sup>k,j</sup>, M. Cepeda<sup>i</sup>, P. Chacon<sup>j</sup>, S. Chacon<sup>j</sup>, L. Chavez<sup>j</sup>, T. Cote<sup>j</sup>, C. D'Agostino<sup>a</sup>, A. Datta<sup>k</sup>, K. DeBlasio<sup>k</sup>, L. DelMonte<sup>f</sup>, E.J. Desmond<sup>a</sup>, J.M. Durham<sup>j</sup>, D. Fields<sup>k</sup>, M. Finger<sup>b</sup>, C. Gingu<sup>f</sup>, B. Gonzales<sup>f</sup>, J.S. Haggerty<sup>a</sup>, T. Hawke<sup>f</sup>, H.W. van Hecke<sup>j</sup>, M. Herron<sup>f</sup>, J. Hoff<sup>f</sup>, J. Huang<sup>j</sup>, X. Jiang<sup>j</sup>, T. Johnson<sup>i</sup>, M. Jonas<sup>f</sup>, J.S. Kapustinsky<sup>j</sup>, A. Key<sup>k</sup>, G.J. Kunde<sup>j</sup>, J. Kurtz<sup>k</sup>, J. LaBounty<sup>a</sup>, D.M. Lee<sup>j</sup>, K.B. Lee<sup>j</sup>, M.J. Leitch<sup>j</sup>, M. Lenz<sup>a</sup>, W. Lenz<sup>a</sup>, M.X. Liu<sup>j</sup>, D. Lynch<sup>a</sup>, E. Mannel<sup>a</sup>, P.L. McGaughey<sup>j</sup>, A. Meles<sup>l</sup>, B. Meredith<sup>c,d</sup>, H. Nguyen<sup>f</sup>, E. O'Brien<sup>a</sup>, R. Pak<sup>a</sup>, V. Papavassiliou<sup>l</sup>, S. Pate<sup>l</sup>, H. Pereira<sup>e</sup>, G.D.N. Perera<sup>l</sup>, M. Phillips<sup>k</sup>, R. Pisani<sup>a</sup>, S. Polizzo<sup>a</sup>, R.J. Poncione<sup>g</sup>, J. Popule<sup>h</sup>, M. Prokop<sup>j</sup>, M.L. Purschke<sup>a</sup>, A.K. Purwar<sup>j</sup>, N. Ronzhina<sup>f</sup>, C.L. Silva<sup>j</sup>, M. Slunečka<sup>b</sup>, R. Smith<sup>g</sup>, W.E. Sondheim<sup>j</sup>, K. Spendier<sup>k</sup>, M. Stoffer<sup>j</sup>, E. Tennant<sup>l</sup>, D. Thomas<sup>k</sup>, M. Tomášek<sup>h</sup>, A. Veicht<sup>c,d</sup>, V. Vrba<sup>h</sup>, X.R. Wang<sup>l</sup>, F. Wei<sup>l</sup>, D. Winter<sup>c,d</sup>, R. Yarema<sup>f</sup>, Z. You<sup>j</sup>, I. Younus<sup>k,2</sup>, A. Zimmerman<sup>k</sup>, T. Zimmerman<sup>f</sup>

<sup>a</sup> Brookhaven National Laboratory, Upton, NY 11973-5000, USA<sup>b</sup> Charles University, Ovocny trh 5, Praha 1, 116 36, Prague, Czech Republic<sup>c</sup> Columbia University, New York, NY 10027, USA<sup>d</sup> Nevis Laboratories, Irvington, NY 10533, USA<sup>e</sup> Dapnia, CEA Saclay, F-91191, Gif-sur-Yvette, France<sup>f</sup> Fermi National Accelerator Laboratory, Batavia, IL 60510, USA<sup>g</sup> Hytec Inc., Los Alamos, NM 87545, USA<sup>h</sup> Institute of Physics, Academy of Sciences of the Czech Republic, Na Slovance 2, 182 21 Prague 8, Czech Republic<sup>i</sup> Lawrence Berkeley National Laboratory, Berkeley, CA 94720, USA<sup>j</sup> Los Alamos National Laboratory, Los Alamos, NM 87545, USA<sup>k</sup> Department of Physics and Astronomy, University of New Mexico, Albuquerque, NM 87131, USA<sup>l</sup> New Mexico State University, Las Cruces, NM 88003, USA

## ARTICLE INFO

## Article history:

Received 19 November 2013

Received in revised form

19 February 2014

Accepted 8 April 2014

Available online 19 April 2014

## Keywords:

RHIC

PHENIX

FVTX

Silicon detector

## ABSTRACT

A new silicon detector has been developed to provide the PHENIX experiment with precise charged particle tracking at forward and backward rapidity. The Forward Silicon Vertex Tracker (FVTX) was installed in PHENIX prior to the 2012 run period of the Relativistic Heavy Ion Collider (RHIC). The FVTX is composed of two annular endcaps, each with four stations of silicon mini-strip sensors, covering a rapidity range of  $1.2 < |\eta| < 2.2$  that closely matches the two existing PHENIX muon arms. Each station consists of 48 individual silicon sensors, each of which contains two columns of mini-strips with 75  $\mu\text{m}$  pitch in the radial direction and lengths in the  $\phi$  direction varying from 3.4 mm at the inner radius to 11.5 mm at the outer radius. The FVTX has approximately 0.54 million strips in each endcap. These are read out with FPHX chips, developed in collaboration with Fermilab, which are wire bonded directly to the mini-strips. The maximum strip occupancy reached in central Au–Au collisions is approximately 2.8%. The precision tracking provided by this device makes the identification of muons from secondary vertices away from the primary event vertex possible.

\* Corresponding author.

E-mail address: [mbrooks@lanl.gov](mailto:mbrooks@lanl.gov) (M.L. Brooks).<sup>1</sup> Present address: Physics Department, University of Michigan, Ann Arbor, MI 48109-1040, USA.<sup>2</sup> Present address: Physics Department, Lahore University of Management Sciences, Lahore, Pakistan.

The expected distance of closest approach (DCA) resolution of 200  $\mu\text{m}$  or better for particles with a transverse momentum of 5 GeV/c will allow identification of muons from relatively long-lived particles, such as D and B mesons, through their broader DCA distributions.

Published by Elsevier B.V.

## 1. Introduction

A new silicon tracking detector has been developed and installed in the PHENIX detector at the Relativistic Heavy Ion Collider (RHIC). Since RHIC began operations in 2000, it has provided collisions of p, d, Cu, Au, and U nuclei at center of mass energies up to  $\sqrt{s_{NN}} = 200$  GeV for heavy ions and 510 GeV for protons. Measurements of the matter formed at RHIC have given evidence that a phase transition to a deconfined state of nuclear matter, the quark gluon plasma, is achieved in ultrarelativistic collisions of large nuclei [1–4]. In addition, RHIC is the world's only collider capable of providing polarized p+p collisions, which can give information on the substructure and spin decomposition of the proton [5].

The PHENIX experiment is a multipurpose detector stationed at the 8 o'clock position on the RHIC ring [6]. The two central spectrometer arms of the PHENIX detector can make measurements of photons and electrons, as well as identified pions, kaons, and protons, while the forward and backward arms contain specialized detectors for tracking and identifying muons. The existing muon arms cover the full azimuthal angle over a pseudorapidity range of  $1.2 < |\eta| < 2.2$ , and consist of a hadron absorber in front of three cathode-strip chambers for charged particle tracking, followed by alternating layers of steel absorber and larocci streamer tubes that function as muon identifiers. Finally, resistive plate chambers (RPCs) provide further muon identification and a fast muon trigger. A diagram of the 2012 PHENIX detector configuration is shown in Fig. 1.

Production of heavy charm and bottom quarks at forward rapidity is of particular interest to the RHIC heavy ion and spin physics programs. Open heavy flavor hadrons at forward angles are measured at PHENIX through their semi-leptonic decays to muons; however, such measurements are limited by systematic uncertainties due to the large backgrounds from  $\pi^\pm$  and  $K^\pm$  decay muons, and hadrons which penetrate the absorbers [7,8]. Also, without precise knowledge of the event and decay vertices, the contributions from D and B meson decays cannot be separated. Quarkonium measurements in the dimuon channel suffer from large combinatorial backgrounds in A+A collisions, which limit the precision of the extracted yields. Since the tracking stations are located behind the hadron absorber, muons undergo multiple scattering in the absorber material before any measurement occurs. This scattering affects the measured opening

angle of the muon pairs, which in turn degrades the mass resolution of dimuon resonances.

The Forward Silicon Vertex Detector (FVTX) enhances the capabilities of the existing PHENIX muon arms by adding additional tracking in front of the hadron absorbers. The four tracking stations of the FVTX add precision vertexing capability to the existing muon spectrometers, with full azimuthal coverage and, when combined with the central silicon vertex detector [9], a rapidity coverage of  $1.2 < |\eta| < 2.2$ . By identifying tracks which originate away from the primary interaction vertex, the FVTX enables rejection of muons which result from decays of relatively long lived particles like  $\pi^\pm$ ,  $K^\pm$ , and  $K_L^0$  when searching for heavy quark and  $W^\pm$  decay muons. In addition, muons from decays of hadrons containing open heavy flavor are identifiable through their broad DCA distributions, and prompt muon pairs from the Drell–Yan process can be tagged as originating from the primary collision vertex. With precision tracking in front of the absorber, the opening angle of muon pairs can be measured before any additional scattering occurs, giving a more precise dimuon mass resolution and enabling the separation of the  $\psi(2s)$  peak from the larger  $J/\psi$  peak in the dimuon mass spectrum. In A+A collisions, the FVTX can also be used to determine the reaction plane.

This paper presents a comprehensive report on the design, construction, and first operation of the FVTX. A general overview of the detector is given in Section 2. Section 3 describes the sensor and electronics associated with processing and reading out the data. Section 4 details the mechanical design of the detector and related infrastructure, and explains how various detector components were assembled. The effects of radiation on the FVTX silicon sensors are discussed in Section 5, and Section 6 shows the initial performance of the detector during RHIC's 2012 and 2013 run periods. Finally, a summary of the paper is given in Section 7.

## 2. Detector overview

The FVTX detector system is composed of two identical endcap sections, located on either end of a four-layer barrel silicon vertex detector (VTX) [9], and in front of the north and south muon spectrometer arms. Each endcap has four layers of active silicon

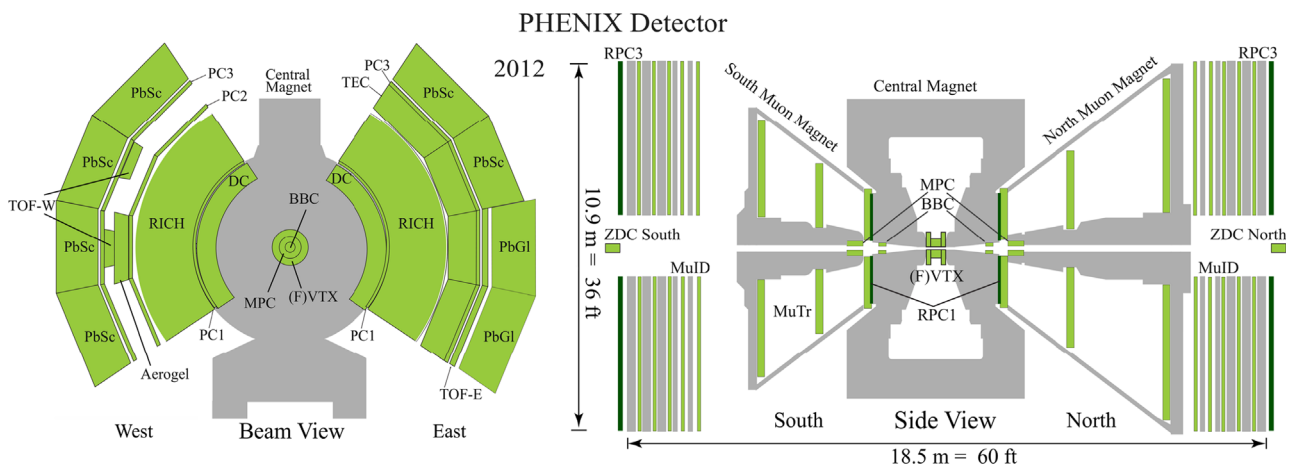


Fig. 1. The 2012 PHENIX detector configuration.

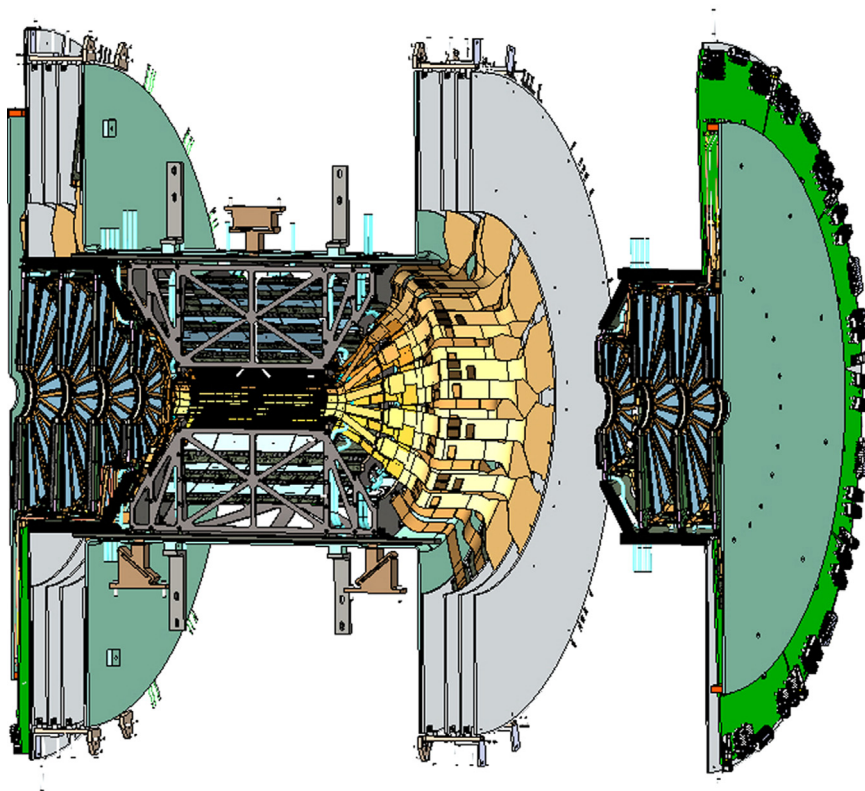


Fig. 2. A drawing of the combined VTX/FVTX assembly. One FVTX quadrant is displaced for clarity.

sensors arranged in a disk around the beryllium beam pipe. The basic unit of construction is a *wedge*, (Section 4.1) each of which carries a mini-strip silicon sensor (Section 3.1), read-out chips (Section 3.2), and a high-density interconnect (HDI, Section 3.3). Wedges are mounted on *half-disks* (Section 4.2), and fitted with extension cables (Section 3.4). For simplicity, the half-disks are referred to as *disks*. Disks are mounted into *cages* (Section 4.3), and the extension cables are connected to *ROC boards* (Section 3.5), the Read-Out Cards that are the first stage in the data path. Finally the cage+ROC assembly is installed in the carbon-composite frame which also contains the VTX components.

Fig. 2 shows a model of two quadrants of the detector, with one FVTX quadrant displaced in  $z$  for clarity. The wedges, mounted on the disks, are shown installed into their cages. The VTX and its associated electronics are shown in the middle, mounted in the support frame. As can be seen in the figure, each cage has one small and three large disks. The smaller disks are simply truncated versions of the larger disks. A summary of the FVTX design parameters is given in Table 1.

### 3. Electronics

This section describes the electrical components and support systems used to read out and power the FVTX. The silicon mini-strip sensors and the FPHX read-out chips are described in Sections 3.1 and 3.2, respectively. The HDI that provides power, bias voltage, and slow control signals to the sensor is discussed in Section 3.3, and the extension cables which handle signals between the wedges and the Read-Out Cards are described in Section 3.4. The Read-Out Cards and Front End Modules which process signals from the detector are discussed in Section 3.5, followed by a description of the high- and low-voltage delivery systems in Section 3.6.

#### 3.1. Sensors

The silicon mini-strip sensors were designed at Los Alamos and fabricated by Hamamatsu Photonics KK. The wedge-shaped geometry comprises two individual columns of strips that are mirror images about the center line on the same sensor. The wire bond connections between the strips and read-out chips are located along the outer edges of the sensor (see Fig. 3). The centerline gap between columns is  $100\ \mu\text{m}$  and is completely active.

The strip length increases with radius on the sensor, and goes from 3.4 mm at the inner radius to 11.5 mm at the outer radius, with a pitch of  $75\ \mu\text{m}$  in the radial direction. Each sensor covers  $7.5^\circ$  in  $\phi$ , and since the strips are perpendicular to the radius, they make an angle of  $86.25^\circ$  with respect to the centerline, as can be seen in Fig. 4.

The sensors were fabricated with p-implants on a  $320\ \mu\text{m}$  thick n-type substrate. The strips are AC-coupled and biased through individual  $1.5\ \text{M}\Omega$  polysilicon resistors to a typical operating voltage of  $+70\ \text{V}$ . The metallization on the strips is wider than the implant to provide field plate protection against micro-discharges, a concern that becomes greater with radiation-induced increases in the leakage current. The strips are also protected by two p-implant guard rings and an  $\text{n}^+$  surround between the guard rings and the sensor edge. There are two sets of bond pads for each strip, one of which is dedicated to probe tests. Each strip also has a spy pad, which is an opening through the capacitor oxide layer, that allows the DC characteristics of the strip to be probed. Fig. 4 shows details of the sensor layout, including guard rings, bond pad locations, and mechanical fiducial marks.

#### 3.2. FPHX chip

A custom 128-channel front-end ASIC, the FPHX, was designed by Fermilab for the FVTX detector [10,11]. The chip was optimized

for fast trigger capability, a trigger-less data push architecture, and low power consumption. The chip was fabricated by the Taiwan Semiconductor Manufacturing Company (TSMC) with 0.25  $\mu\text{m}$  CMOS technology. The analog section consists of an integrator/shaper stage followed by a 3-bit ADC. A single FPHX chip mounted onto the HDI is shown in Fig. 5. In this example, the wire bonding to the control lines on the HDI is complete, but no bonding between the sensor and the chip has been performed.

Many of the setup parameters of the front end are programmable via an LVDS serial slow control line. Adjustable parameters include gain, threshold, rise and fall time, input transistor bias current, channel mask, plus several additional fine tuning parameters. Nominal setup parameter values include integrator/shaper gain of 100 mV/fC, 800 mV dynamic range, 60 ns risetime at the shaper output, and a 2000-electron threshold at the first comparator. All analog functions were exercised on a test stand and the measured values were very close to pre-submission simulations.

The FPHX chip was designed to process up to four hits within four RHIC beam crossings (or  $\sim 4 \times 106 \text{ ns} = 424 \text{ ns}$ ). Each hit

contains a 7-bit time stamp, a 7-bit channel identifier, and a 3-bit ADC value. By only accepting hits above a certain (programmable) ADC threshold, the signal-to-noise ratio can be dynamically optimized for different operating conditions. In addition, the ADC information from strips in an FVTX hit cluster is used to determine the center of the track via a weighted average of the charge in each strip. An ADC with higher resolution would not significantly improve the detector's tracking resolution, since multiple scattering in detector material is the dominant contribution to track smearing at the  $\sim 20 \mu\text{m}$  level.

The data words are output over two LVDS serial lines at up to 200 MHz clock rate. The total power consumption of the FPHX is  $\sim 390 \mu\text{W}$  per channel. The noise, when the chip was wire bonded to a sensor with strips  $\sim 2\text{--}11 \text{ mm}$  in length ( $\sim 1\text{--}2.5 \text{ pF}$ ), was simulated and measured to be below the design specification of 500 electrons.

### 3.3. High-density interconnects

The silicon sensor and FPHX read-out chips are assembled on an HDI which provides the slow control, power, and bias input lines as well as slow control and data output lines. The HDI stack-up is shown in Fig. 6 and consists of seven layers of single-sided (20  $\mu\text{m}$ ) and double-sided (50  $\mu\text{m}$ ) copper coated polyamide bonded together with a 25  $\mu\text{m}$  sheet adhesive for a total thickness of approximately 350  $\mu\text{m}$ . Indicated on the HDI stack-up are two

**Table 1**  
Summary of design parameters.

Silicon sensor thickness ( $\mu\text{m}$ )	320
Strip pitch ( $\mu\text{m}$ )	75
Nominal operating sensor bias (V)	+70
Strips per column for small, large wedges	640, 1664
Inner radius of silicon (mm)	44.0
Strip columns per half-disk (2 per wedge)	48
Mean z-position of stations (mm)	$\pm 201.1$ , $\pm 261.4$ , $\pm 321.7$ , $\pm 382.0$
Silicon mean z offsets from station center (mm)	$\pm 5.845$ , $\pm 9.845$

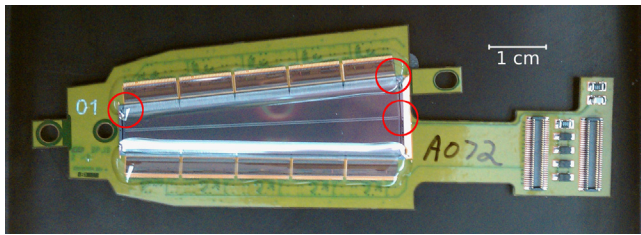


**Fig. 3.** A completed FVTX small wedge, with sensor facing up. Note the center line dividing the two halves of the sensor and rows of FPHX chips along the sensor edges.

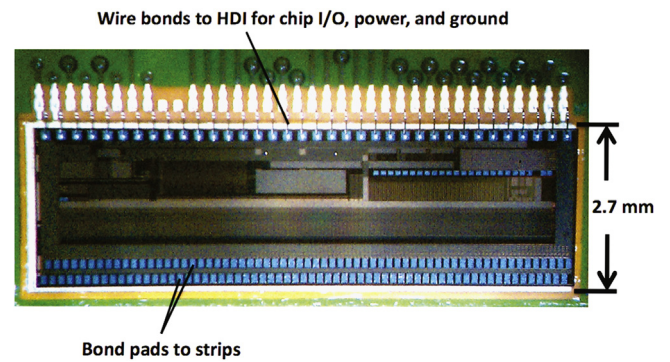


**Fig. 5.** A single FPHX chip mounted onto the HDI. Along the top, wire bonds to the HDI have been completed. Along the bottom, in two rows, are 128 bond pads for wire bonds to the silicon strips.

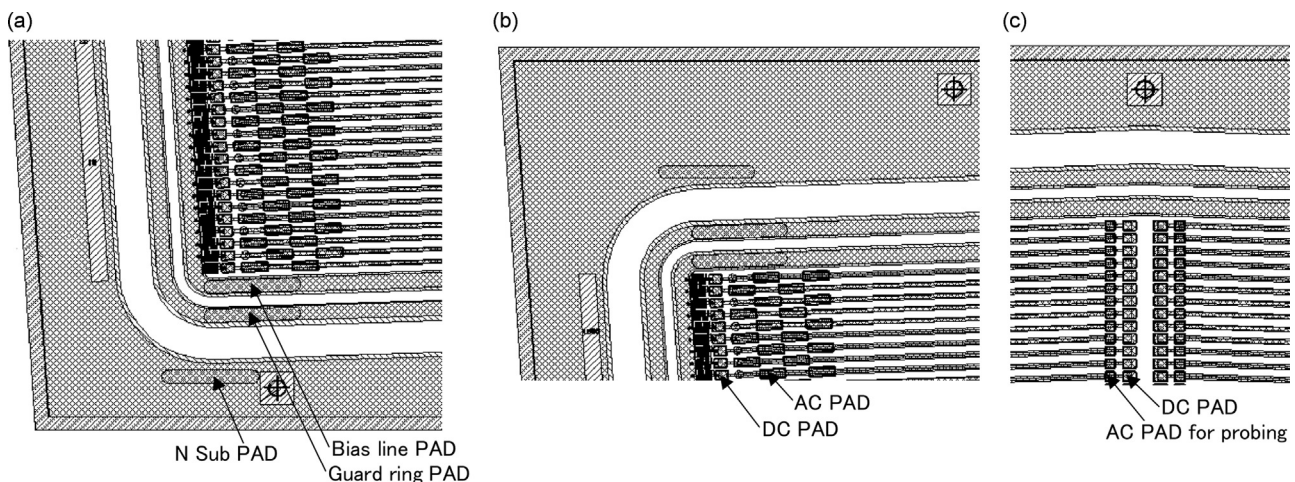


**Fig. 4.** Details of the sensor layout. (a) Narrow end corner, (b) wide end corner and (c) wide end center. These areas correspond to the circled regions in Fig. 3.

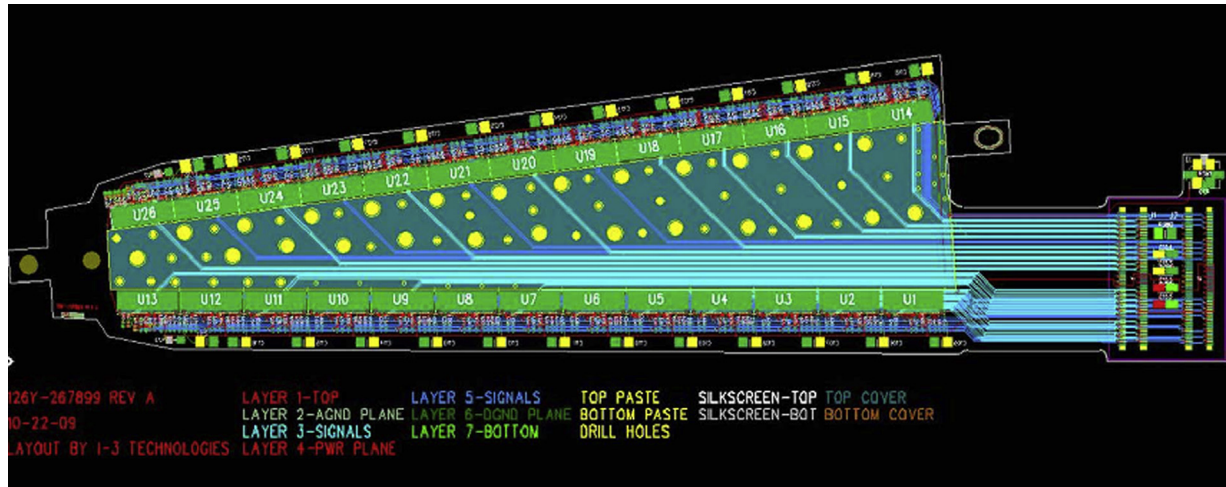


Fig. 6. Schematic of the HDI stack-up.

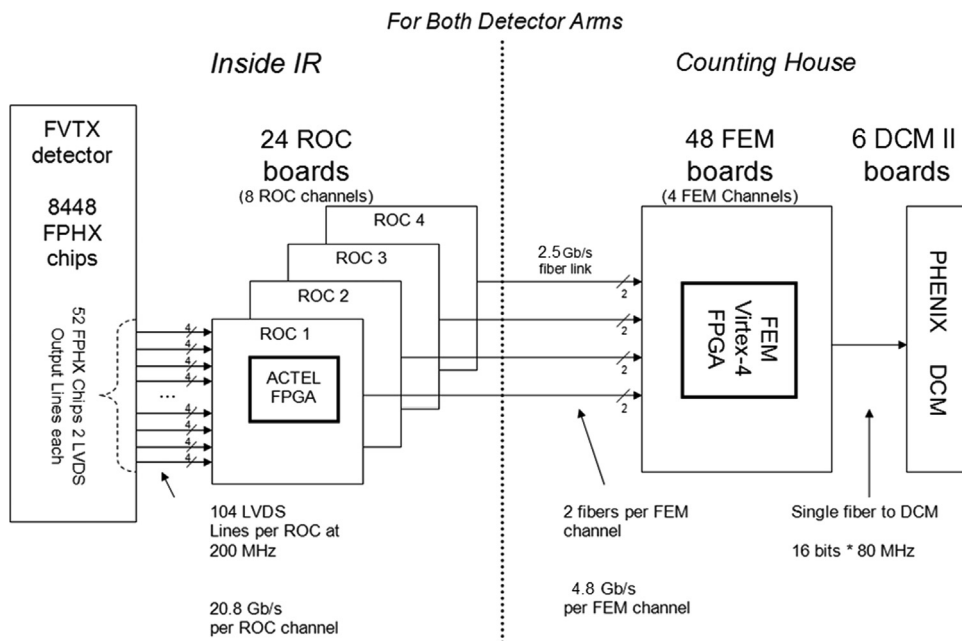


Fig. 7. Read-out electronics block diagram.

signal layers, one ground layer, and one power layer. All control lines (which are not active during data taking) are routed under the sensor, and all output lines are routed towards the edge of the wedge, thus minimizing the coupling between the output lines and the sensor. The number of lines (8 pairs for the control lines and 2 signal pairs per chip for the output lines) requires that they have a  $40\ \mu\text{m}$  width with a  $100\ \mu\text{m}$  spacing. Both simulated and physical tests were carried out to ensure that the input clock (200 MHz) had sufficient integrity at the furthest point from the driver.

Since the layout of the wedge, chip, and HDI can impact the system noise, the electrical layout of the wedge assembly was designed to minimize any additional noise. Incorporated onto the HDI were two noise-canceling loops, one for the input side and one for the output side of the chip, employing bypass capacitors connected to the bias ground and the digital ground, respectively. Termination resistors for the calibration lines and bias resistors and capacitors are also located on the board. All elements are surface mounted and assembled by the manufacturer (Dyconex and Micro Systems Engineering).

### 3.4. Extension cables

The extension cables were designed to bring all signals from the HDI to the ROC board and power from the ROC board to the wedge, and have a similar stack-up design to the HDIs. The mechanical layout of the extension cables was unique for each side and each disk of the FVTX to allow the ROC end of the extension cables to precisely line up to the corresponding connector on the ROC. Both the HDI and the extension cables needed to be permanently bent in multiple directions in order to precisely fit them within the constraints of the detector envelope. Bending was accomplished using fixtures which bent the flex circuits and heated them at  $100\ ^\circ\text{C}$  for  $\sim 5$  min, in order to introduce a permanent deformation.

### 3.5. ROCs/FEMs

The design of the read-out electronics for the FVTX detectors is based on three major constraints, imposed by the detector:

- Large instantaneous bandwidth (3.38 Tb/s).

- Radiation hardness of read-out components near the interaction point.
- Large number of I/O lines (21 000 LVDS pairs).

As a result, the read-out electronics are logically divided into two independent blocks, illustrated in Fig. 7. The components are the following:

- *Read Out Card (ROC)*: Module which is located close to the detector.
- *Front End Module (FEM)*: Module which is located in the Counting House (~50 m from the Interaction Region) in a standard VME crate.
- *FEM Interface Board*: Module located in each of the FEM VME crates.

The output of the FEM connects to the standard PHENIX DAQ board, a Data Collection Module (DCM), and from this point on the data stream becomes a part of the standard PHENIX DAQ.

### 3.5.1. Read Out Card (ROC)

The ROC boards are mounted on an aluminum cooling plate and connected to the HDIs through the extension cables. Since the board has components on both the top and bottom surfaces, a 1/8 in. thick layer of soft non-conductive Gap-Pad material is placed between the ROC boards and the cooling plate in order to facilitate heat transfer.

The ROC boards are designed to

- Receive data via LVDS pairs from the silicon read-out chips.
- Combine and synchronize the data streams from multiple FPHX chips.
- Send the data to the Front End Module (FEM) in the counting house via optical fibers.
- Receive and distribute slow control data to/from the FPHX chips and other ROC components.
- Hold an on-board calibration system for the FPHX chips.
- Hold an on-board JTAG FPGA which allows for remote programming of the slow control and data FPGAs.

The ROC board design utilizes radiation-hard FLASH-based ACTEL ProASIC3E FPGAs in order to limit susceptibility to single event upsets (SEUs). A functional ROC board diagram is shown in Fig. 8. Each board contains four large-scale ACTEL A3PE3000-FG896 FPGAs to process the data from the read-out chips, 33 16-bit Serializer/Deserializer chips (TLK2711) and four 12-channel optical fiber transmitters (HFBR-772BEZ) to send the data to two FEM boards. Each ROC FPGA holds two completely independent ROC channels, for a total of eight ROC channels per board, which send out 32-bit data at the output clock frequency of 125 MHz. The outgoing data are logically split into two hi/lo 16-bit data portions which are each sent to separate Serializer/Deserializer chips and a single fiber channel. A small-scale ACTEL FPGA is dedicated to distributing slow control signals to appropriate chips and reading data back, to be sent up the slow control data stream to the FEM. Slow control data are sent by the FEM to the ROC and by the ROC to the FEM over a single optical fiber interface. Another small-scale ACTEL FPGA provides an interface between the slow control fiber and on-board FPGAs, to allow remote programming of the slow control and data FPGAs.

The Beam Clock (9.4 MHz) arrives at the ROC board as an LVDS signal and is distributed to all the FPGAs on the board as well as to all the FPHX chips. A Serial Clock of  $20\times$  the Beam Clock frequency is generated by a PLL on the slow control FPGA. The output data from the FPHX chips are phase latched to a similarly

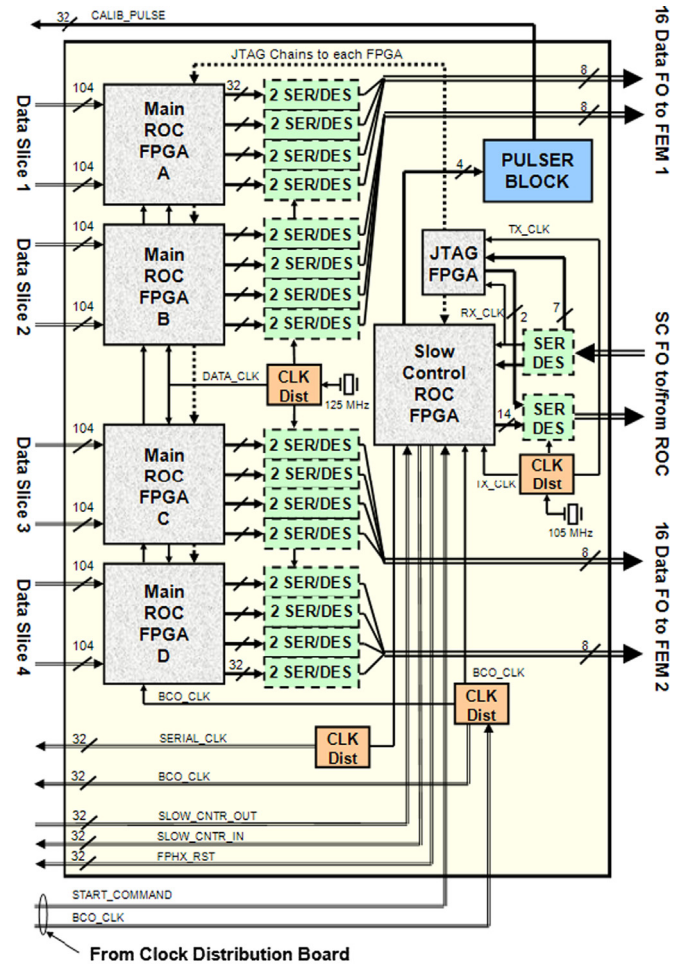


Fig. 8. Block diagram of the ROC board.

generated  $20\times$  clock inside the Main FPGAs, which avoids distribution of the fast clock between FPGAs and simplifies the design.

A schematic of a single ROC channel is shown in Fig. 9. The main task is to combine data from up to 10 FPHX chips into a single data stream without any delay: 20-bit data deserialization gives time for this. Three of those streams are combined by a 3-to-1 Round-Robin Arbiter and buffered into a 256 deep output FIFO. We utilize triple redundancy on every component that allows for it, and actively use design blocks for predictable layout and timing. The design is latch free by construction, with constant synchronization of the input serial data streams.

The ROC board includes a calibration system that can deliver a precisely controlled voltage pulse to each FPHX chip on an HDI. The signal injection timing is synchronized with the Beam Clock. A 10 bit dual DAC is used together with a precision reference and analog switches to provide a large dynamic range and low noise. The amplitude is adjustable via the slow controls, while a fast rise and a slow fall time are fixed by RC circuits. The calibration system is used routinely to check for dead FPHX channels and determine the electronics noise levels. When disabled, the system contributes negligible noise to the FPHX chips.

### 3.5.2. ROC radiation environment

The primary consideration when evaluating FPGA technology available for use on the ROC was the effect of the radiation

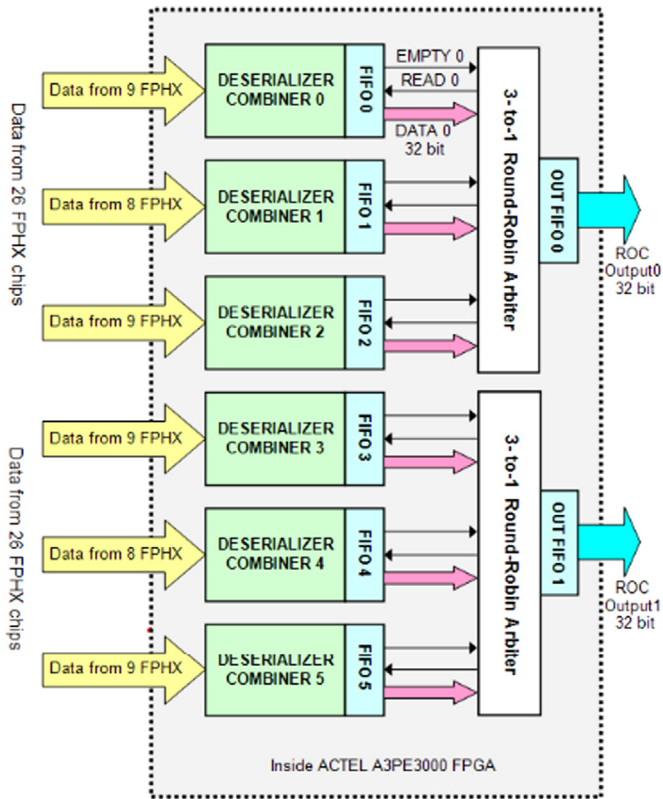


Fig. 9. Block diagram of a single ROC channel and a single 10-chip channel deserializer/combiner.

environment on the performance of the system. Additional considerations included I/O configurations, serial communication capabilities, and the ability to reconfigure the device within the

system. The choice is primarily the selection of configuration memory technology, as logic implementation and density have minimal impacts in this application. The different configuration technologies and their suppliers that were considered are as follows:

- SRAM Altera, Xilinx;
- FLASH Actel ProASIC3;
- Anti-fuse Actel Axcelerator.

The primary elements of the FPGA that are affected by the radiation are the SRAM memory elements, clocks, and sequential logic. Since the configuration of Altera and Xilinx FPGAs is contained in SRAM, upsets in this memory will affect functionality of the device. Both Xilinx and Altera offer configuration “scrubbing” solutions that check the configuration, but they require a reload of the configuration if an error is detected, which takes time. The Actel FPGAs do not have SRAM configuration memory so they are immune to this form of upset, which is a distinct advantage. The Actel ProASIC3 was chosen. In the 2012 and 2013 runs at RHIC, no problems due to radiation effects on the ROC FPGAs were observed.

### 3.5.3. Front End Module (FEM)

The FEM boards are located in 6U VME crates in the counting house (in a shielded location ~50 m from the detector) where radiation levels are negligibly small and SRAM-based FPGAs can be used. The FEM boards are functionally designed to

- Receive data from the ROC boards over fiber links.
- Sort the incoming data according to the Beam Clock Counter.
- Buffer the data from the last 64 beam clocks.
- Upon Level-1 trigger decision, ship the data from the Beam Clock of interest to the output buffer, which ships data to the PHENIX Data Collection Modules (DCM).
- Distribute and receive slow control data to/from the ROC cards. The online slow control interface is made through the FEM Interface Board and the interface to the ROC cards is made through an optical fiber.

The FEM board architecture can be seen in Fig. 10. Xilinx Virtex-4 FPGAs are used as the main FEM FPGA. The largest device of the memory-intensive SX series (XC4V5X55) provides enough fabric and memory to implement four FEM channel cores and a channel combiner on a single FPGA. This significantly reduced the cost of the FEM board design.

A block diagram of a single FEM channel and FEM channel combiner is shown in Fig. 11. One FEM board receives 16 optical fibers (from half of a ROC board). The incoming 16-bit data nibbles from the ROC are aligned and combined into 32-bit data words; alignment bits are used in transmission. Data are buffered for 64 beam clocks in each of the four FEM channels in an array of 64 512 word deep FIFOs. Each FIFO stores the data for a particular beam bucket (0 through 63). Since data from the FPHX chips carry the 7-bit beam clock counter information, the sorting is trivial.

Upon receiving a Level-1 trigger, the FEM channels start sending the data from a particular beam bucket of interest to the output sub-event buffer. The internal clock speed for reading and writing is 300 MHz in order to minimize latencies in the design. The resulting sub-events are combined and packetized in the “Channel Combiner” block into 16-bit wide packets. Packets carry fixed data (Event Counter, BCO Counter and Longitudinal Parity) in header and trailer words. The design is implemented using Xilinx RPM blocks and directed routing concepts. The current version of the design can run at up to 350 MHz clock on a –10 speed grade

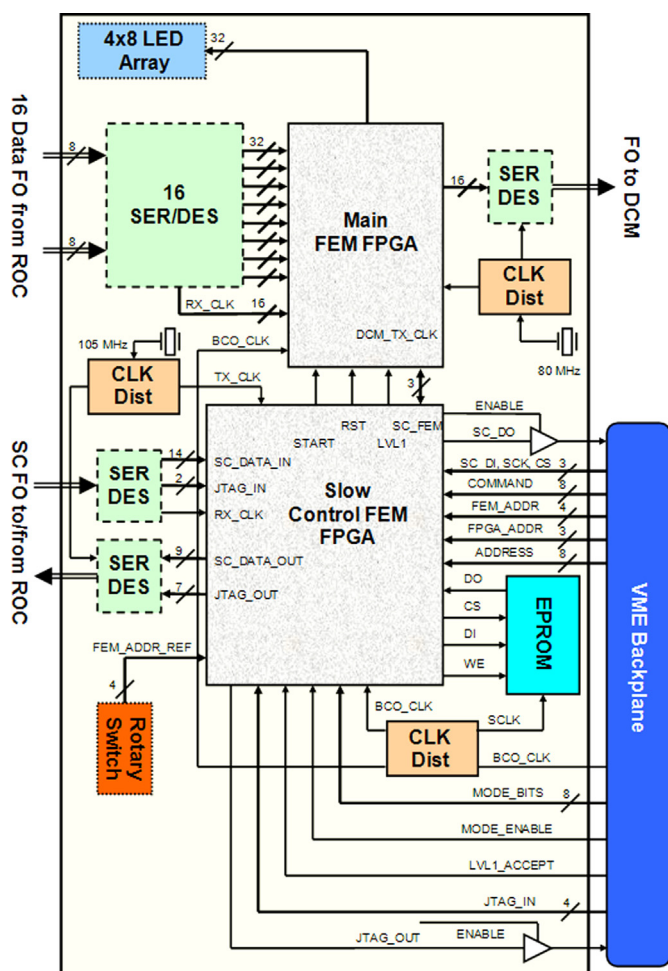


Fig. 10. Block diagram of a FEM board.

FPGA. The Floorplanner diagram of the current implementation is shown in Fig. 12. A separate small-scale FPGA (Spartan3 XC3S200) processes incoming timing signals and slow control commands. Timing and fast control signals in PHENIX are distributed through a specially designed Granular Timing Module (GTM). The GTM signals include the Beam Clock, a Level-1 Trigger and Control Mode Bits. These signals are copied to the main FEM FPGA and the beam clock is selected out by the FEM Interface Board and sent to the ROC board.

#### 3.5.4. FEM Interface Board

Each VME Crate with 12 FEM boards is controlled by a single 6U FEM Interface Board which acts as a simple crate controller and is designed to

- Receive GTM (beam clock and trigger) signals.
- Distribute the information from the GTM to the FEMs via the VME backplane.
- Distribute the Beam Clock to a set of ROCs via a front-panel fiber optic interface.
- Distribute a START signal to a set of ROCs via a front-panel, to allow the FEM and ROC read-outs to be synchronized.
- Interface to the PHENIX Online slow controls system via Ethernet or USB, and to the FEM boards via the VME backplane.

The FEM Interface Board utilizes a commercial MOD5270 Motorola Coldfire Ethernet Daughter Board and FT2232 USB Module to

provide a bi-directional slow control data stream, and also holds a PHENIX standard G-Link Receiver board. The full block diagram of a FEM Interface Board is shown in Fig. 13.

#### 3.6. Detector bias, low voltage, and grounding

Each detector wedge requires independent 2.5 V digital and analog power sources as well as a bias supply. Thus, 768 DC supply channels and 384 bias channels are needed for the full FVTX detector. In addition, each ROC uses a number of moderately high power DC sources to operate the boards. Bulk DC power is provided by Vicor MegaPACs. These high-power switching supplies are connected to modules in a low voltage DC power crate system designed at BNL. Each module provides 10 channels of up to 10 A DC output, with independently monitored voltage and current. Power for the ROC cards is wired directly to these outputs. Low voltage distribution crates were designed to fan out these high current channels to all of the wedges. The power to each wedge is individually enabled via Ethernet slow controls. The distribution cards have individual fuses per wedge and filter each DC source and return line using pi networks.

A Wiener Mpod system serves as the bulk supply for detector bias voltage. It provides 48 low current channels with adjustable voltage and current readback through Ethernet. Another distribution crate was designed to fan out these channels to each wedge, controlled by Ethernet. Each output is protected against over voltage using zener diodes. The source and return lines are filtered as described above. The typical bias voltage applied to each sensor during operation is +70 V.

##### 3.6.1. Grounding system

A star topology was chosen for the overall grounding plan. At the center of the star is each wedge/HDI. The wedge bias, FPHX analog and digital grounds are tied together only at their respective HDIs. The digital grounds are returned to the ROC cards through the wedge extension cables, which are all tied together and earthed to the PHENIX central magnet. Electrically filtered distribution boards, described in the previous section, prevent ground loops and noise from being introduced by the remote power and bias supplies.

## 4. Mechanical design

Here we describe the mechanical design of the FVTX and the procedures used to assemble the various components into a complete detector. The assembly of the silicon sensors, FPHX chips, and HDI into a wedge is explained in Section 4.1. The disks which hold the wedges and the cages which house the disks are described in Sections 4.2 and 4.3, respectively. The cooling system used to remove heat generated by the detector electronics is described in Section 4.4, and the environmental enclosure that is necessary to avoid condensation on the cooled electronics is discussed in Section 4.5.

### 4.1. Wedges

A wedge is the basic construction unit of the FVTX detector. Fig. 14 shows an exploded view of a single wedge assembly, which consists of a silicon mini-strip sensor (Section 3.1), FPHX read-out chips (Section 3.2), a high-density interconnect bus (HDI, Section 3.3), and a carbon support backplane.

Assembly of wedges took place at the SiDet Facility at Fermilab. A series of precision assembly fixtures were used to affix the HDI onto the backplane, to place the FPHX read-out chips on the HDI+backplane assembly, and finally to attach the silicon sensor

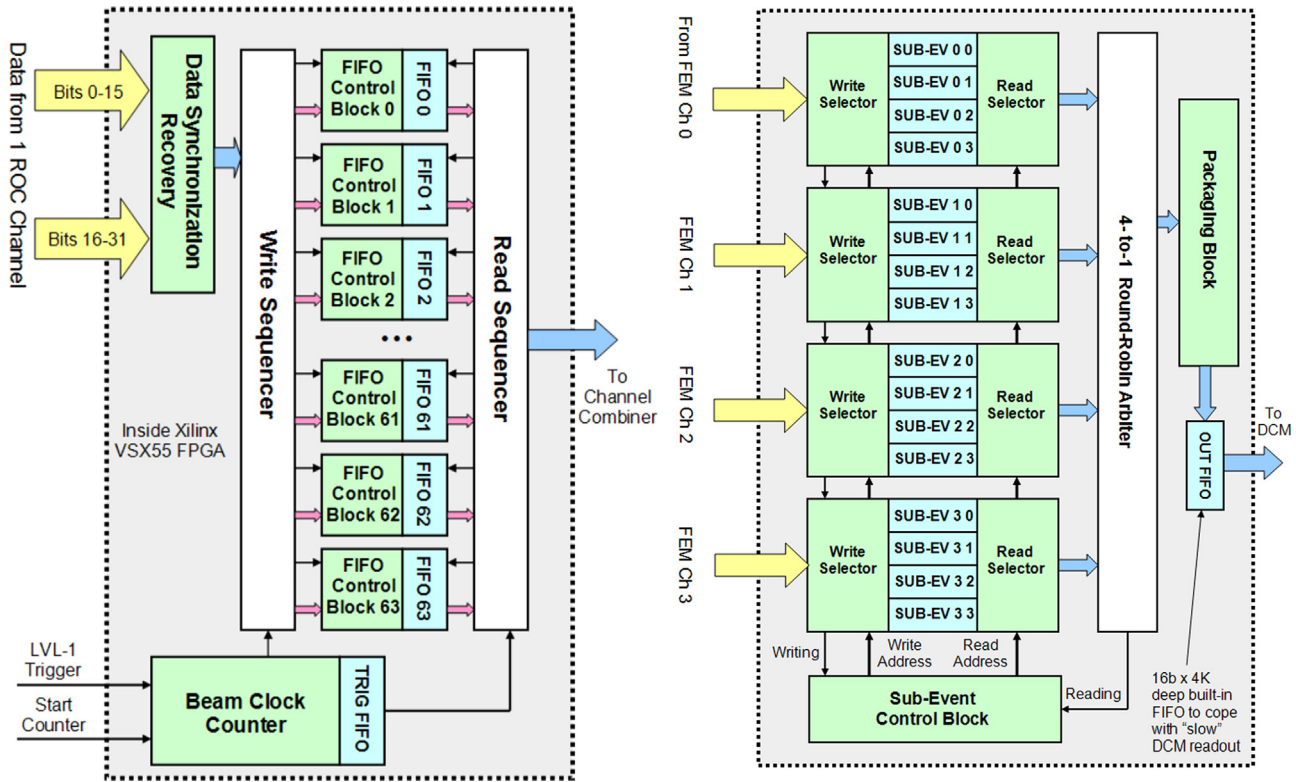


Fig. 11. Block diagram of a single FEM channel and a channel combiner.

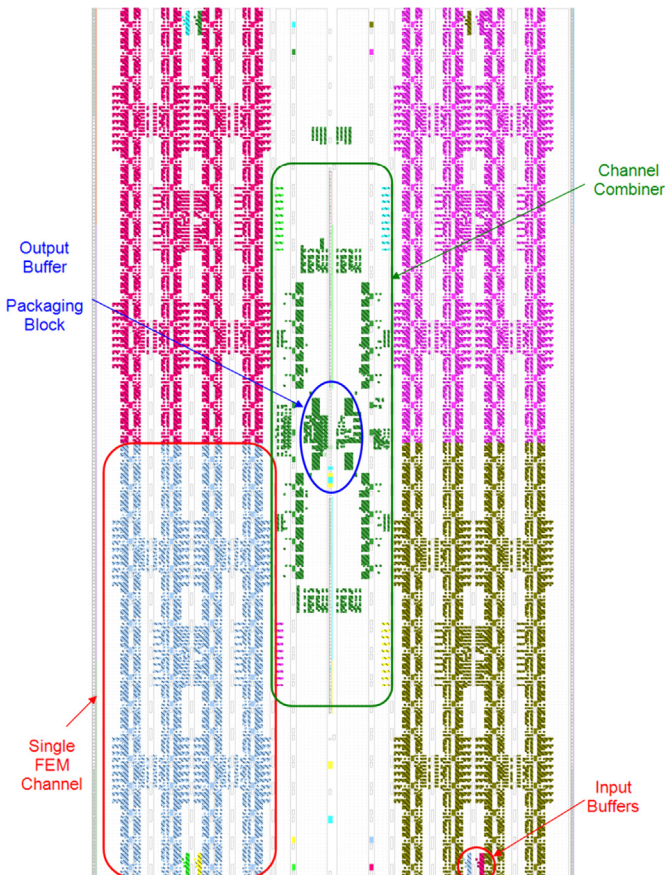


Fig. 12. Implementation of the FEM FPGA design.

to the chip+HDI+backplane stack. At each assembly step, two fixtures used vacuum to hold the relevant components in place. Pins and holes on the fixtures aligned the components as they were brought together, and pressure was applied between the two fixtures to ensure complete bonding between the components and the adhesive. Fig. 15 shows a wedge assembly in progress.

The carbon support backplane is formed from K13D2U carbon fiber (Mitsubishi Chemical) bonded with EX1515 (Tencate Advanced Composites) resin, with a total thickness of 1.56 mm. Using the assembly fixtures, the HDI was glued onto the carbon backplane using Arclad 7876 [12], a 50 μm-thick dry adhesive. The thin, seven-layer HDI circuit was populated with passive electronic components and connectors prior to mounting on the backplane.

After the HDI and backplane were assembled, a different set of assembly fixtures was used to place the FPHX chips in position on the HDI. Large wedges have 13 chips on each side, while small wedges have 5. After placement the chips were wire bonded to the HDI and tests were performed to ensure proper function. A similar procedure was then used to attach the silicon sensor to the chip+HDI+backplane assembly with Arclad adhesive. Silver epoxy (TRA-DUCT 2902 from Tra-Con) was used to connect the silicon's bias voltage surface to the HDI. Next, wire bonds were made between the sensor and the read-out chips. A suite of tests was then performed on the completed unit to ensure proper functioning of the wedge. After this the wire bonds were encapsulated with Dow Corning Sylgard 186 for protection. Completed wedge assemblies were then shipped to Brookhaven National Laboratory for final preparation and installation.

Further operations were needed before a wedge was ready to be mounted onto the disk support plane. A small ground wire was attached with conductive silver epoxy to a small hole in the carbon plane, and connected to ground on the HDI. This serves to drain off charge that may build up on the carbon backplane. Next, graphite

## FEM INTERFACE BOARD Block Diagram

6/24/2009

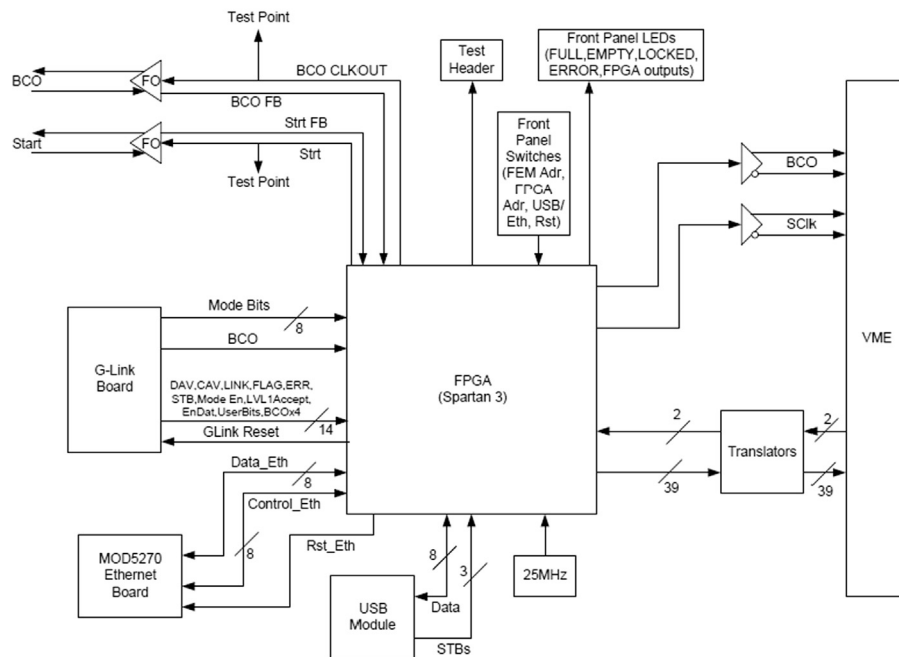


Fig. 13. Block diagram of the FEM Interface Board.

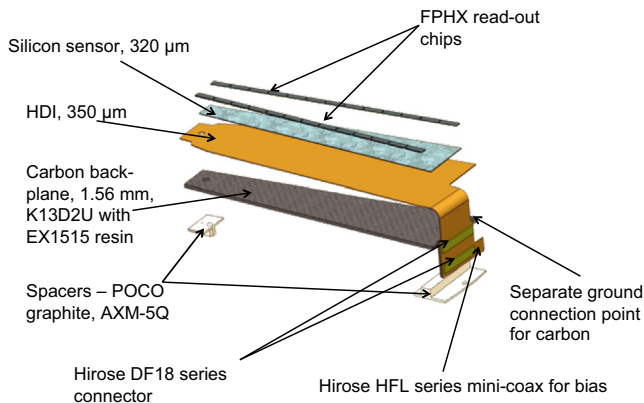


Fig. 14. Exploded view of an FVTX sensor assembly.

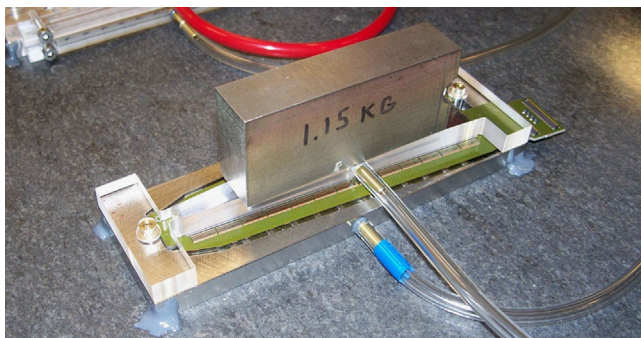


Fig. 15. Assembly fixtures in use. At this step, the silicon sensor is being placed onto the FPHX chip + HDI + backplane assembly.

feet (Poco Graphite) were glued to the underside of the carbon plane. Finally, the HDI was bent through  $90^\circ$  near the connector end using a thermal bending apparatus that heated the kapton-copper HDI to  $100^\circ\text{C}$ , in order to permanently form it to match the cage shape.

### 4.2. Disks

The wedge support disks are flat sheets of 0.4 mm thick thermally conductive carbon fiber (K13C2U from Mitsubishi Chemical) on both sides of a carbon-loaded PEEK plastic frame. The PEEK at the outer radius contains a cooling channel, with nylon hose barb fittings at the ends, which removes heat generated by the FPHX chips. PEEK buttons maintain the spacing between the face sheets. Fig. 16 shows an exploded view of a disk assembly.

On both faces of the disks, precision alignment pins are located along the inner and outer radii, one pair for each wedge which will be mounted on the disk. These pins match a precision hole and slot in the graphite feet of the wedges, assuring placement of the wedges onto the support disk with an accuracy of  $25\ \mu\text{m}$ . Wedges are secured onto the disk with small PEEK screws near each of the alignment pins.

The silicon sensor on each wedge subtends an angle of  $7.5^\circ$ . Adjacent wedges on a disk overlap in the azimuthal direction by 0.5 mm to give hermetic coverage in the azimuthal direction. Since the HDI is significantly wider than the silicon sensor, the wedges must be staggered in  $z$  to allow this continuous azimuthal coverage by the sensors. This is achieved by mounting wedges on both sides of the disks, at alternating  $z$  positions on each side. The graphite feet on the back of the wedges come in two varieties so that wedges can be alternately mounted at 0.9 mm or 4.9 mm above the surface of the disk. During assembly, the disk was mounted on the precision mount points into an assembly frame. The frame allowed one to work on the disk assembly in any orientation. In addition, aluminum cover sheets could be mounted on the outside of the assembly frame, turning it into a storage and transportation box, as shown in Fig. 17.

After each disk was fully populated with wedges, the positions of the wedges were precisely measured by Hexagon Metrology using an optical coordinate measuring machine. Fiducial marks, four on each silicon detector, were measured with an accuracy of  $5\ \mu\text{m}$  in the plane of the silicon, relative to the three precision mounting points on the perimeter of the disk.

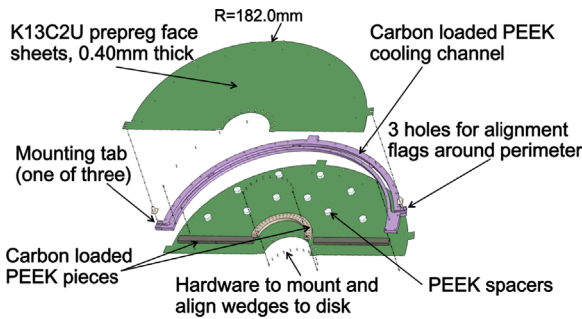


Fig. 16. Exploded view of a support disk.

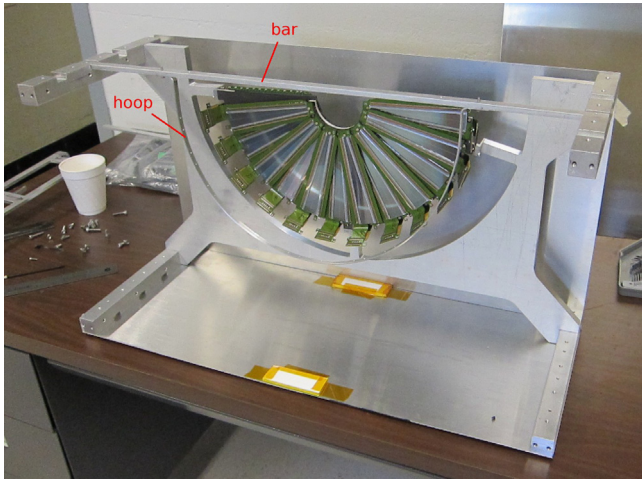


Fig. 17. A populated disk in its support frame. Some of the cover sheets are in place. The hoop will support the extension cables that will be connected to the wedges prior to installation in the cage.

Before a disk was mounted into a cage, a temporary transfer fixture was fitted to the centerline of the disk. Extension cables (Section 3.4) were connected to the wedges, as well as bias voltage coaxial cables and disk cooling tubes. The transfer fixture also supported these cables. At this point, the disk was disconnected from its three precision mount points on the assembly frame and was transferred into a cage.

The disks were mounted into a cage on the three precision mount points located on the outer radius of the disk. To maximize the detector's  $\phi$  resolution, each of the four disks are mounted into the cage offset in  $\phi$  by an angle  $3.75^\circ/4$  with respect to the neighboring disk.

#### 4.3. Cages

The cages, into which disk assemblies are mounted, are carbon-composite structures fabricated from CN60 carbon fabric (Nippon Graphite Fiber) with EX1515 resin. One of these cages is shown in Fig. 18 with four mounted disks (without wedges). During construction, the cage was mounted in an assembly structure that also supported the aluminum cooling plate onto which the ROC boards (6 per quadrant) are mounted, as shown in Fig. 19. A soft material (Gap-Pad by the Bergquist Company), approximately 1/8 in. thick, is placed between the ROC and the cooling plate to improve heat transfer. Each disk is mounted into a cage on three mount points, each of which has an alignment pin and a screw. First the small disk was mounted, and extension cables connected to the ROC boards, followed by the three large disks in turn. At the inner radius of the ROC boards, pairs of connectors can be seen, one pair

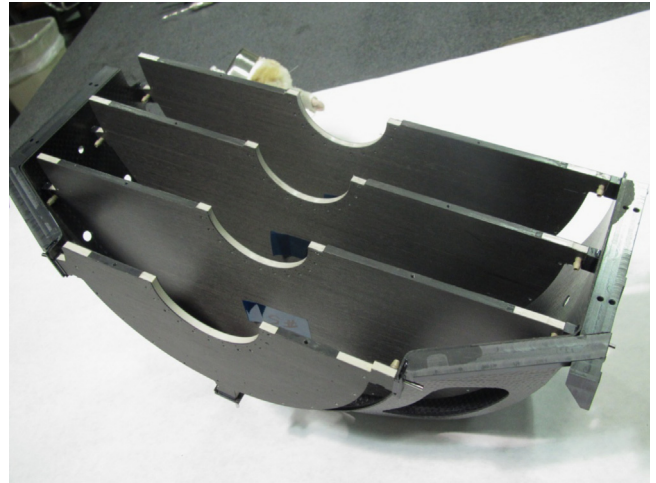


Fig. 18. A cage with all four disks installed. No wedges have been placed on the disks.

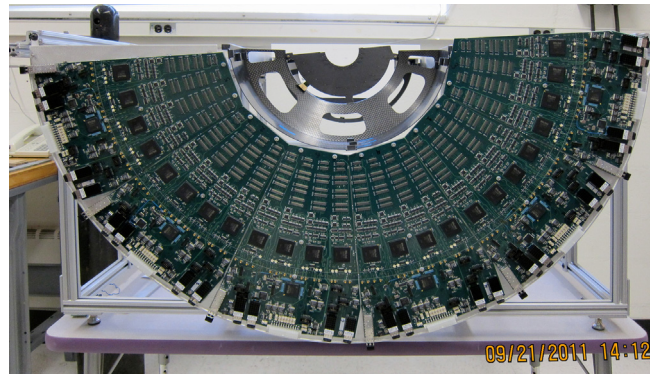


Fig. 19. A cage and ROC boards on an assembly frame. An unpopulated small disk is mounted at the rear of the cage.

for each wedge/extension cable. A completed half-detector is shown in Fig. 20.

During the selection for the support materials several factors were considered: low radiation length is desirable to minimize interactions in detector materials; high rigidity is necessary for maintaining alignment and stability of detector components; ease of machining and availability are important for construction. Candidate materials for the FVTX support structures were beryllium, glass fiber reinforced polymer, and carbon-carbon composite.

The wedge backplanes were constructed from K13D2U prepreg with EX1515 resin, 1.56 mm thick. This fiber was selected because of its good thermal conductivity, which is necessary to remove heat generated by the FPHX read-out chips. For the 0.4 mm thick disk face sheets, K13C2U prepreg with EX1515 resin was chosen because it is widely available, works well in sandwich composites, and has a small radiation length and favorable strength properties. For similar reasons, the cage was made from 6 plies of CN-60 cloth, for a thickness of 1.5 mm.

The vibrational mode frequencies, gravitational load distortions, and shape changes with temperature were studied for all mechanical structures, and used to verify that the dimensional stability requirements were met.

#### 4.4. Cooling

Heat generated by the FPHX chips on the wedge assemblies amounts to  $390 \mu\text{W}/\text{channel}$ , or 1.3 W for a large wedge. The heat is conducted from the chips to the HDI, through the wedge carbon

backplane, through the graphite feet to the skin of the support disks, and finally to the cooling channel at the outer radius of the disks. With the cooling channel located at the outer radius of the wedge, a temperature gradient of  $\sim 4^\circ\text{C}$  is developed across the length of the wedge during normal operation.

The ROC cards are mounted onto a 1/8 in. aluminum plate, with approximately 1/8 in. of Gap-Pad in between. These plates are

cooled via chilled fluid circulation through an aluminum tube dip-brazed to the outer edge of the plate.

The cooling system for the FVTX consists of two identical closed loops operated at different temperatures. One loop provides  $0^\circ\text{C}$  cooling fluid to the disks that the wedges are mounted on, while the other provides  $10^\circ\text{C}$  fluid to the aluminum cooling plates holding the ROC boards. The systems are composed of a chiller (stainless wetted parts), stainless steel transfer lines, and a manifold and flow control system, with short PTFE and Tygon tubing section where flexibility is required. The system also has a continuously running parallel cleaning loop to remove contaminants. The detector and the manifold system are located inside our interaction area and are inaccessible while the collider is operating. Because of this, a remote monitoring and interlock system was developed to prevent detector damage in the case of accidental loss of cooling. A schematic of one of the systems is shown in Fig. 21.

The coolant used in the system is Novec 7200 (ethoxy-nona-fluorobutane) manufactured by 3M [13]. Novec 7200 is an engineered fluid that was developed as both a heat transfer fluid and a cleaning fluid. Novec 7200 is clear, non-conductive, non-corrosive, low odor, and a low toxicity fluid that has zero ozone-depletion potential. In addition, it has very low greenhouse gas properties, and can be used as a heat transfer fluid in the temperature range  $-138^\circ\text{C}$  to  $76^\circ\text{C}$ . The coolant leaves no residue behind when it evaporates. These characteristics make it very

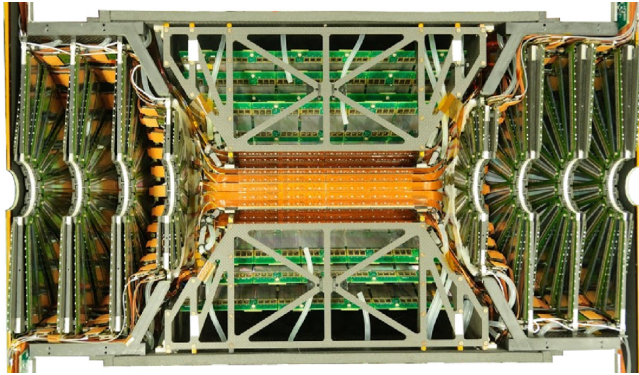


Fig. 20. A completed half-detector, with the VTX barrels in the center, and the two VTX endcaps on either end. The overall length is 80 cm.

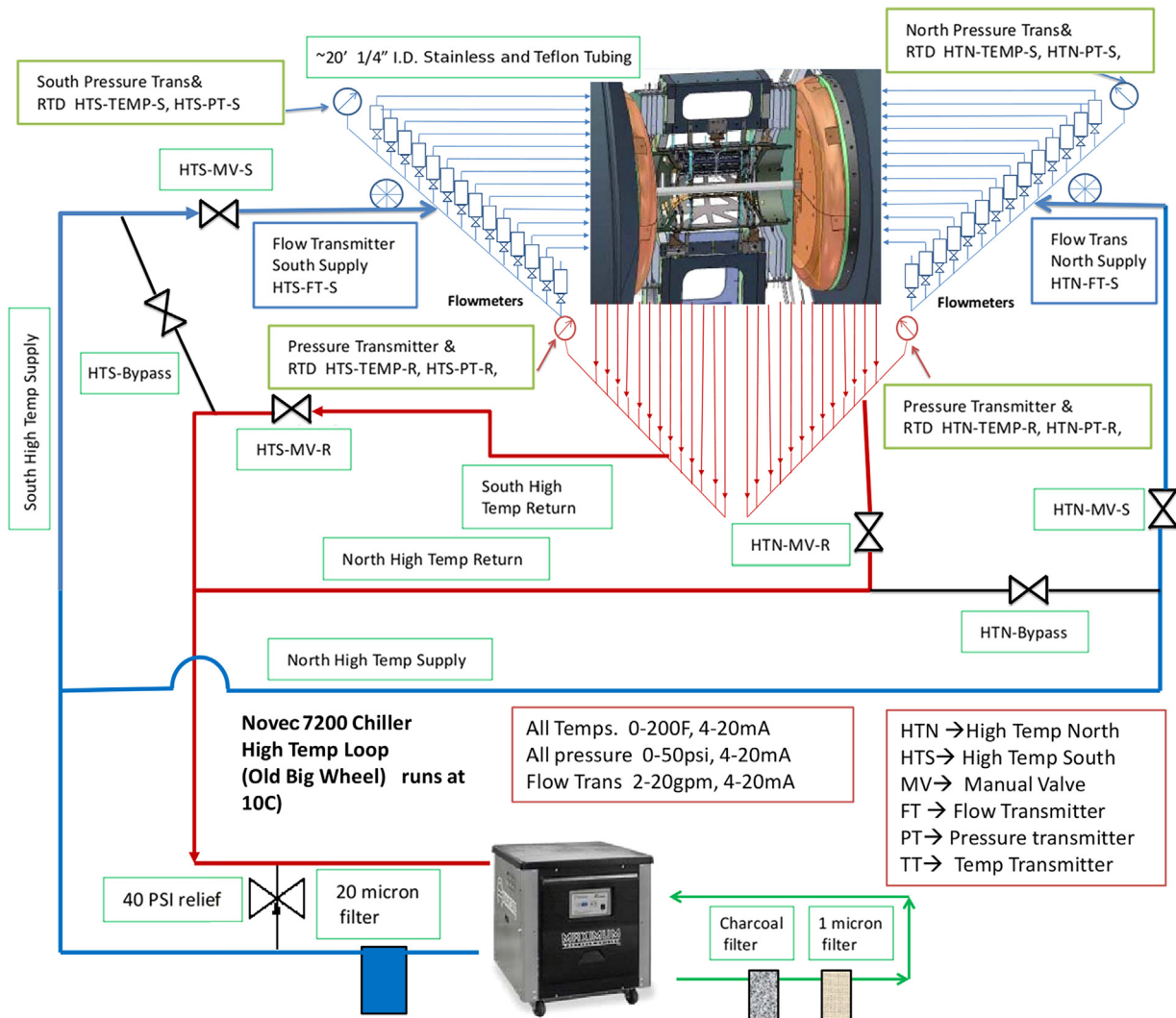


Fig. 21. Schematic of one FVTX cooling loop.

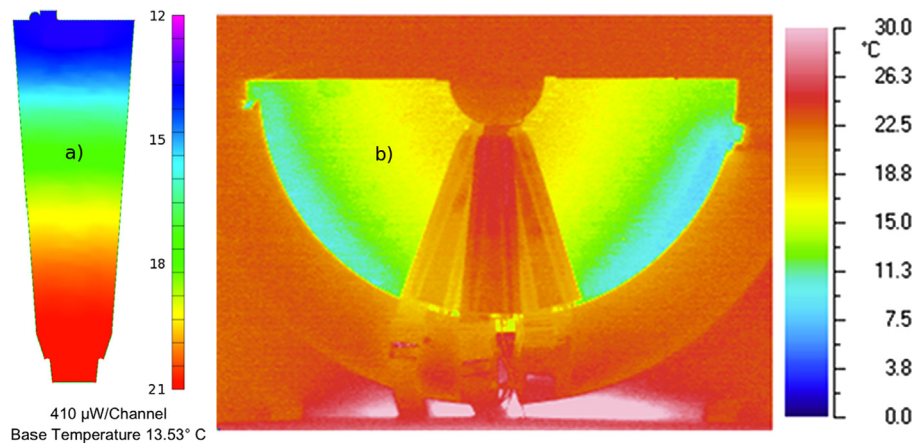


Fig. 22. Calculated (a) and measured (b) temperature distribution of a wedge, powered and mounted on a disk, with cooling turned on.

attractive from an environmental and performance standpoint, but introduce several challenges when using it as a cooling fluid.

Because of its cleaning ability, both material compatibility and fluid cleanliness are concerns. Novec 7200 has a low viscosity and a low surface tension. As a result, the fluid will work its way into tight areas and dissolve any surface contaminants. It will also dissolve many plasticizers and components of soft materials, so proper selection of wetted materials should be made. Any contaminants left in the fluid can then leave a residue on a surface in the event of a system leak. Because of this, it was found that the fluid must be cleaned while in operation to prevent contaminant buildup. This is achieved by continuously routing a small portion of the coolant through a charcoal column.

Another concern with the fluid is its electronegativity and triboelectric charging while flowing through a non-conductive material. Problems arose where static charge built up in Tygon and PTFE tubes. The resulting discharges created pinhole leaks through 1/32 in. PTFE tube walls. This can be avoided by using only conductive tubing or minimized by reducing the length of non-conductive tubing.

At the design stage, finite element calculations were performed to estimate the temperatures and temperature gradients in the wedges. Fig. 22 shows the expected temperatures on a wedge in the left panel. Since the cooling channel runs along the outer diameter of the support disk, the tip of the wedge is warmer than the broader end. The gradient in this calculation spans about 7 °C. The right panel shows an image taken with a thermal camera of a disk with three wedges mounted, while the wedges are powered and the cooling is running. The measured temperature gradient in the wedges is smaller than in the calculation, about 4 °C.

#### 4.5. Environmental enclosure

The central rapidity silicon vertex detector (VTX) and the two FVTX endcap regions share an environmental enclosure, which is continually purged with dry nitrogen gas during operation to avoid condensation on the cooled electronics. The dry nitrogen is produced by bleeding the boil-off of a large liquid nitrogen dewar through a heat exchanger to raise the temperature of the gas. The enclosure radius is 22 cm in the region of the VTX barrel, and extends to ~50 cm from the beam axis to contain the VTX transition electronic boards and the FVTX ROC boards.

### 5. Radiation effects

Silicon detectors operated in high-radiation environments at colliders can suffer from radiation damage to the bulk silicon,

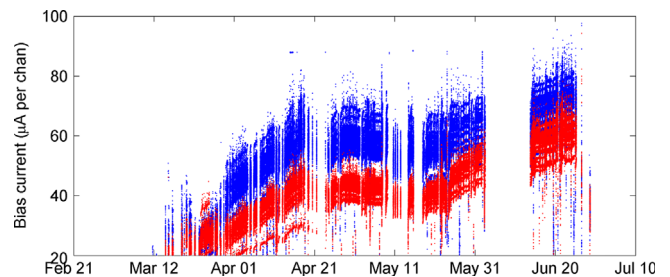


Fig. 23. Current draw as a function of time for the FVTX bias supplies during the 2012 RHIC run. Each point is from the bias supply for a group of eight individual wedges. The North arm is in blue and the South arm is in red. (For interpretation of the references to color in this figure caption, the reader is referred to the web version of this paper.)

resulting in increased leakage currents and noise [14–16]. The FVTX location near the collision vertex exposes the silicon sensors to a significant ionizing radiation flux during beam tuning and data taking. In the 2012 run at RHIC, the FVTX was exposed to radiation from Cu+Au, p+p, and U+U collisions at  $\sqrt{s_{NN}} = 200$  GeV, and p+p collisions at  $\sqrt{s} = 510$  GeV. As expected, significant increases in the wedge leakage currents were observed. Fig. 23 shows the current draw from the FVTX bias power supplies as a function of time during the 2012 run.

In addition to direct radiation produced by colliding beams, secondary radiation induced in material surrounding the FVTX may also contribute to the bulk radiation damage. Specifically, the nosecone pole tip of the PHENIX central magnet, located directly behind the FVTX, is a possible source of secondary electrons, X-rays, and spallation neutrons.

To study the effects of radiation in the actual operating environment of the FVTX, active radiation-monitoring sensors were installed in the PHENIX interaction region during the RHIC run starting in February 2013, which was dedicated to p+p collisions at  $\sqrt{s} = 510$  GeV. The sensors were procured from the Solid-State Radiation Sensor Working Group at CERN. Each PCB carrier (15 mm × 32 mm) was populated with a p-i-n diode, a RadFET, and a temperature probe. The device was monitored by providing a constant current and reading out the required voltage. Sensors were mounted on the nosecone pole tip of the PHENIX central magnet at radial distances ( $r = 3.5, 8.5$  and  $16.2$  cm) corresponding to the inner and outer radii of silicon on the FVTX station disks. During the initial beam tuning, when the VTX/FVTX was positioned several centimeters away from the final position around the beam pipe, two additional sensors were mounted at distances along the beam axis corresponding to the locations of the innermost and outermost FVTX station disks (see Table 1). These

sensors were removed when the FVTX/VTX assembly was closed from the retracted to the operating configuration. A BNL-designed front-end electronics board capable of interfacing with all the sensors facilitated real-time monitoring through the current PHENIX online system. Finally, five passive thermoluminescent dosimeters (TLDs) were mounted at positions corresponding to the CERN sensors to cross check the integrated dose. These were removed when the detector was moved into its operating position.

Fig. 24 shows the integrated dose measured during the tune-up period of the collider, with the detector in the retracted position. Contributions to the integrated dose from individual stores in RHIC are clearly visible. The data exhibit the expected drop in dose as the radial distance from the beam axis increases. More importantly, there is good agreement for the measured dose from gamma radiation between the RadFETs calibrated with a method provided by CERN and the TLDs (labeled TKXXX). Fig. 25 shows the integrated dose measured for the entire 2013 RHIC run from 510 GeV p+p collisions with the remaining three RadFETs on the nosecone poletip. The highest integrated dose is 43 krad for the RadFET ( $1 \times 1 \times 0.5 \text{ mm}^3$ ) at a radial distance of 3.5 cm from the nominal beam axis. This is well under the yearly dose that would limit operation of the FVTX to less than 10 years (under normal operating conditions at RHIC). A similar conclusion can be drawn for the integrated dose from neutrons measured with the p-i-n diodes, which are systematically lower than the dose from gamma radiation measured with the corresponding RadFETs shown in Fig. 25.

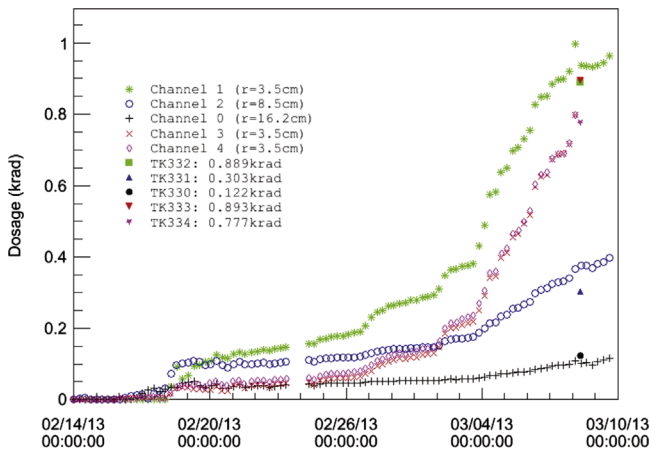


Fig. 24. Integrated dose in the RadFET monitors as a function of time during RHIC beam tuning for the 2013 run. The TLD dose is shown for reference.

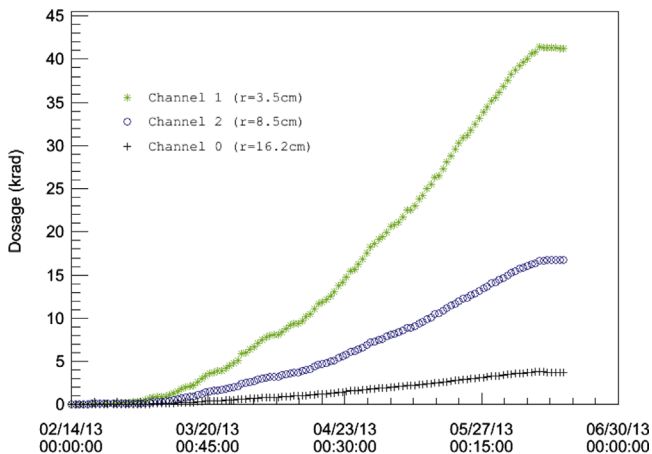


Fig. 25. Integrated dose from the three RadFETs installed on the PHENIX magnet poletip, directly behind the FVTX, measured as a function of time during the 2013 RHIC run.

To quantitatively determine the effect of radiation damage on the FVTX, several FVTX sensors were directly exposed to the 800 MeV proton beam at LANSCE [17]. Pairs of FVTX sensors were mounted in FR4 frames and placed in the beam's path. The dose delivered during the 510 GeV p+p portion of RHIC's Run-12 was taken as a benchmark. During that run, the PHENIX experiment sampled  $30 \text{ pb}^{-1}$  within the nominal 30 cm vertex range. Using measurements of the radiation environment at RHIC from [18], this luminosity corresponds to a delivered dose of  $\sim 1.7 \times 10^{10} N_{eq}/\text{cm}^2$ , where  $N_{eq}$  is the equivalent flux of 1 MeV neutrons. Since the LANSCE beam has a hardness  $\kappa \sim 0.7$ , this corresponds to a flux of  $2.5 \times 10^{10} \text{ p}/\text{cm}^2$ . Pairs of wedges were exposed to 1, 5, 10, and 20 times this dose. During irradiation, the sensors were at room temperature and bias was not applied. The leakage currents of the wedges were measured *in situ* immediately preceding and following beam exposure. Prior to irradiation, all wedges drew less than 20 nA at 100 V.

Fig. 26 shows the leakage current as a function of bias voltage for the sensors after exposure to the LANSCE proton beam. As expected, the leakage currents increased proportionally to the received dose (see Fig. 27). To examine the effects of radiation on the bias voltage required for full depletion, the voltage at which the leakage current is 90% of the plateau value is shown in Fig. 28. Although there may be a small increase in the most irradiated sample, this is well below the typical operating bias voltage of 70 V. A small but detectable amount of residual radiation ( $< 1 \text{ mrem}/\text{h}$  on contact) was observed on the wedges after irradiation, presumably due to activation of various isotopes in the sensors and FPHX chip material. This low amount of residual radiation is not expected to significantly contribute to ongoing damage in the bulk silicon.

It is well established that the electrical characteristics of irradiated silicon vary with time and sensor temperature [19–21]. In the short term, on the scale of weeks to months, a decrease in leakage current due to annealing is expected. Long term effects due to reverse annealing, which happen on the scale of years, can increase the leakage current and bias voltage required for full depletion.

To examine effects from annealing, the leakage currents were measured again for each wedge after 3 weeks. Since the actual FVTX sensors are kept at room temperature in between data taking periods, no temperature excursions were undertaken, as these can affect the annealing properties of silicon. Fig. 29 shows the resulting  $I$ - $V$  curves, after a correction was applied to account for the slight difference in sensor temperature at the time of the second measurement. A significant decrease ( $\sim 40\%$  for each wedge) in the plateau leakage current is observed (see Fig. 30), which is the expected effect of annealing. No large changes in the required bias to reach the plateau of

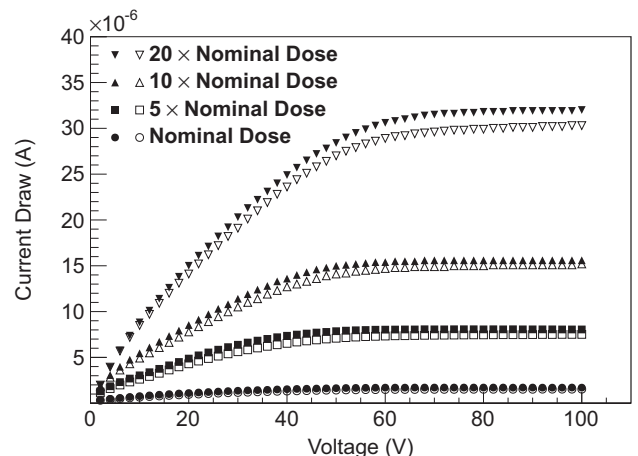


Fig. 26. Leakage current as a function of the applied bias voltage for the test wedges, measured immediately following irradiation.

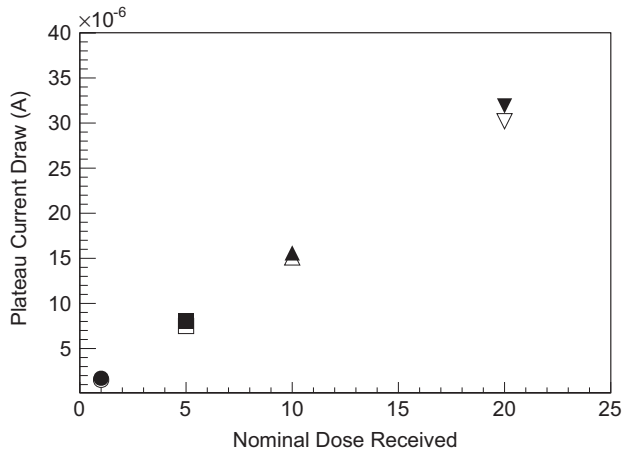


Fig. 27. The plateau values of the leakage current of the irradiated wedges, measured immediately following the irradiation.

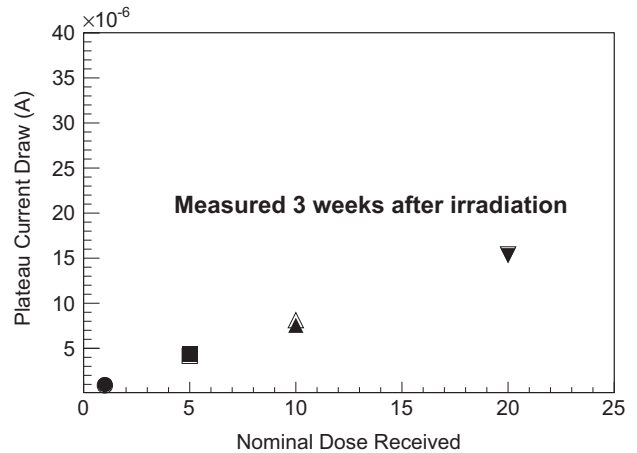


Fig. 30. The plateau values of the leakage current of the irradiated wedges, measured 3 weeks after the irradiation.

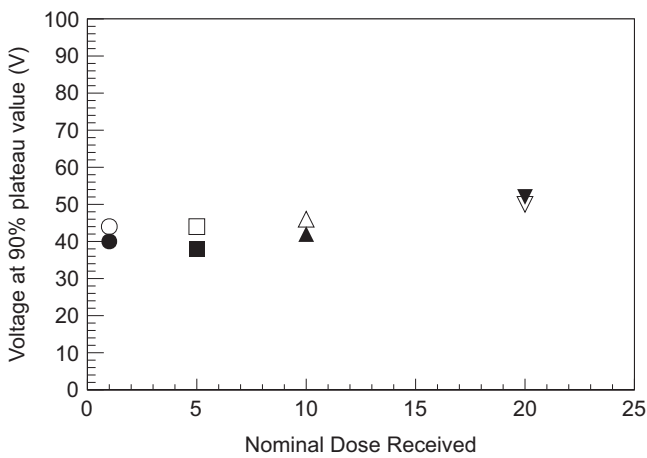


Fig. 28. The applied bias at 90% of the plateau value of the leakage current, measured immediately following the irradiation.

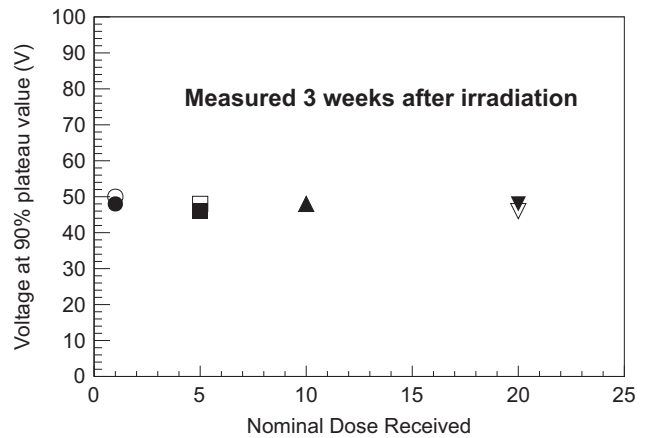


Fig. 31. The applied bias at 90% of the plateau value of the leakage current, measured 3 weeks after the irradiation.

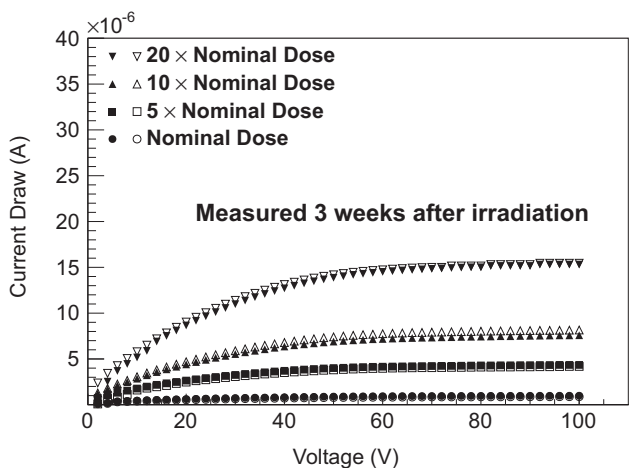


Fig. 29. Leakage current as a function of the applied bias voltage for the test wedges, measured 3 weeks after the irradiation.

the leakage current are observed (Fig. 31). Further studies of the evolution of the leakage current over time are underway, in order to understand the competing effects of annealing and any reverse annealing which may occur.

While the FVTX sensors do show the expected increase in leakage current with the received radiation dose, the magnitude of the increases will not require any changes in the cooling system or bias voltage equipment over the expected life of the experiment.

## 6. Performance

This section presents performance benchmarks from the FVTX, using data collected during operation at RHIC.

### 6.1. Timing

The distribution in time of FVTX hits is studied relative to the RHIC collision time by comparing the hit rate at different FVTX delay values relative to the RHIC beam clock. The timing distribution for two sectors of wedges in the south arm is shown in Fig. 32. Most hits fall in a window  $\sim 30$  ns wide.

Two standard trigger timing configurations were used during FVTX operation, as shown by the vertical lines in Fig. 32: during relatively low trigger rate running (in heavy ion systems) hits arriving in a time window two RHIC beam clocks (BCO) wide (1 BCO  $\sim 106$  ns) are accepted. In high trigger rate p+p running, a 1 BCO-wide window is used to avoid recording accidental hits from neighboring beam crossings (1 BCO apart).

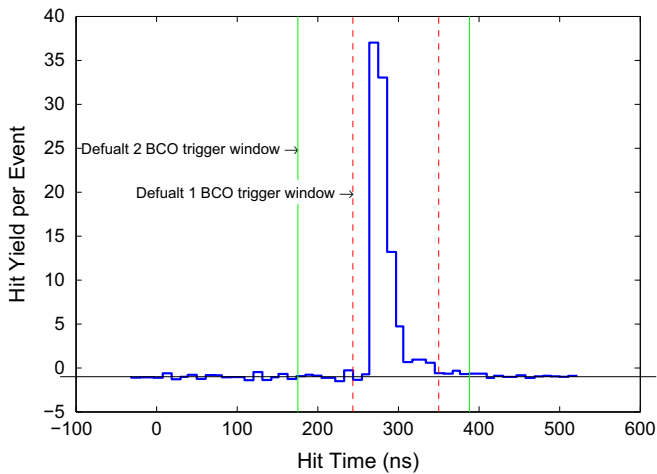


Fig. 32. Timing distribution of the FVTX hits relative to the RHIC beam clock.

### 6.2. Hit Efficiency

Multi-layer tracking detectors require a large intrinsic hit efficiency in each sensor, that is, a high probability that a particle of interest will produce a measured signal when traversing an active sensor layer. To evaluate this efficiency in the FVTX, charged particle tracks which are identified by hits in three of the FVTX stations are projected to the fourth station. A hit cluster in the fourth station at the projected position is assumed to be due to the charged track, which is a good assumption for the low occupancy p+p events used in this study.

The probability of finding a hit at the projected spot in station 2 using tracks identified by hits in stations 0, 1, and 3 is shown in Fig. 33, as a function of the angle  $\phi$  around the disk, using data recorded during the 2013 RHIC p+p run. The extracted efficiencies shown in this plot include the intrinsic efficiency of the detectors as well as any efficiency loss due to dead channels, chips, or DAQ channels. The peak efficiencies are above 95% indicating that the intrinsic efficiency of the detector is quite high. The area near  $\phi=90^\circ$  in the North arm has a low hit efficiency due to a broken component on a ROC board, which prevented several wedges from being read out. However, the overall live area during the 2013 run was greater than 95%.

### 6.3. Alignment and residuals

Misalignment of the silicon wedges relative to each other and multiple scattering of particles as they pass through the FVTX sensor material will have a detrimental effect on the ultimate tracking resolution of the detector. The internal detector alignment was performed using data taken with the PHENIX magnets turned off, so all charged particles travel in straight lines. The MILLEPEDE-II [22] package was used to internally align all detector elements.

After detector alignment was performed, the FVTX single hit resolution was determined with straight-line tracks found in the FVTX, matched with tracks found in the muon spectrometer, from p+p collisions recorded with the PHENIX magnets turned off. These tracks typically have a total momentum  $p > 3$  GeV/c. After finding tracks with hits in three FVTX stations, the track residual for the fourth station is found by calculating the distance between the track projection and the center of the nearest FVTX hit cluster in that station. The width of this track residual distribution is determined by the hit position resolution in each station and the distance between tracking layers. To find the single-particle hit position resolution for a single station, a correction is applied to the track residuals, which was determined from linear regression assuming a common single-particle hit position resolution in the

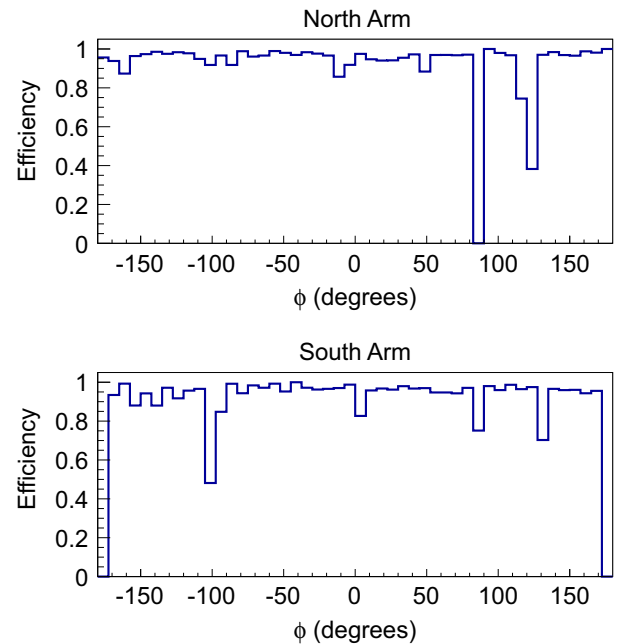


Fig. 33. Hit efficiency for FVTX station 2 as a function of  $\phi$ .

three stations used to find the track and a common distance between the stations. The scaled track residuals, which represent the single-particle hit position resolution, are shown in Fig. 34 for the innermost tracking station in the north and south arms. The position resolution for each of the eight stations varies between 24 and 28  $\mu\text{m}$ , which is within the design parameters.

### 6.4. Electronic noise

The FPHX chip was designed to have a relatively low noise of  $\sim 500$  electrons when wire bonded to the actual FVTX sensor (see Section 3.2). The electronic noise in the detector is monitored periodically using the calibration system. During calibration, groups of 10 signal pulses of a given height are sent to an injection capacitor at the front-end of the read-out chip, while the signal height is scanned across the discriminator threshold. The noise level is characterized by the broadening of the hit efficiency threshold as shown in Fig. 35. A normal cumulative distribution function is used to fit the data. The noise level is parametrized by the width,  $\sigma$ , of the fit function.

A histogram of the noise level for all operating channels is shown in Fig. 36. The average electronic noise level is between 350 and 380 electrons, which is significantly lower than the nominal discriminator threshold of  $\sim 2500$  electrons. This level of electronic noise is well within design parameters of the FPHX chip and read-out system.

## 7. Summary and conclusion

This paper presents a comprehensive report on the design, construction, and operation of a Forward Silicon Vertex Detector, the FVTX, for the PHENIX experiment at RHIC. The detector consists of four layers of silicon mini-strip sensors at forward and backward rapidity, and enhances the capabilities of the existing PHENIX muon arms by providing precision tracking of charged particles before they interact in the hadron absorber. It was first installed and operated at PHENIX prior to the 2012 RHIC run.

The detector active area covers the full azimuthal angle over the forward rapidity range  $1.2 < |\eta| < 2.2$ . Each individual silicon sensor is

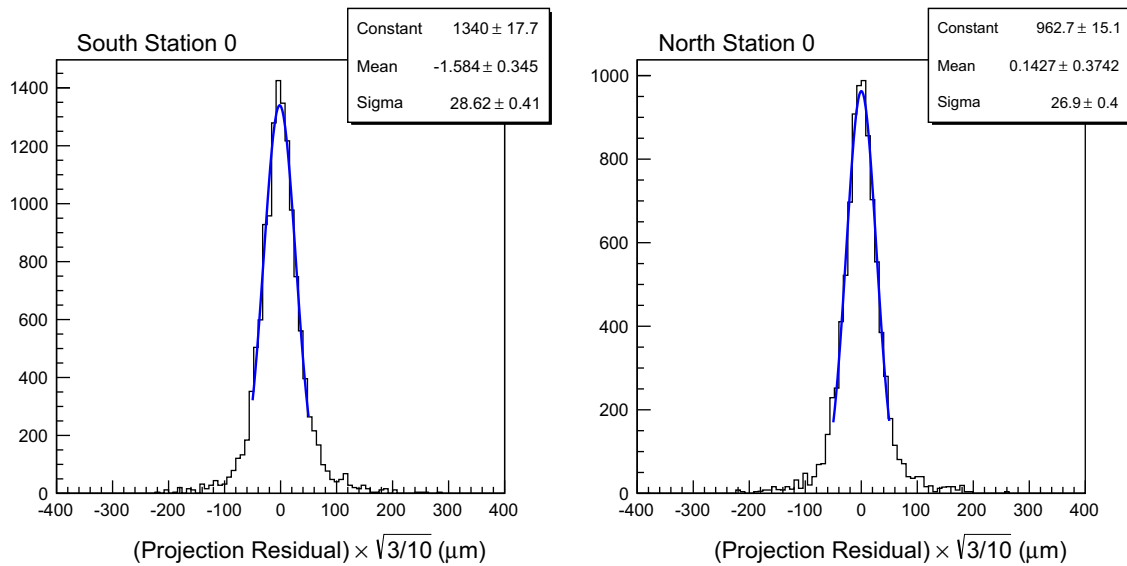


Fig. 34. Track residuals for the innermost FVTX tracking stations, scaled to give the single hit resolution.

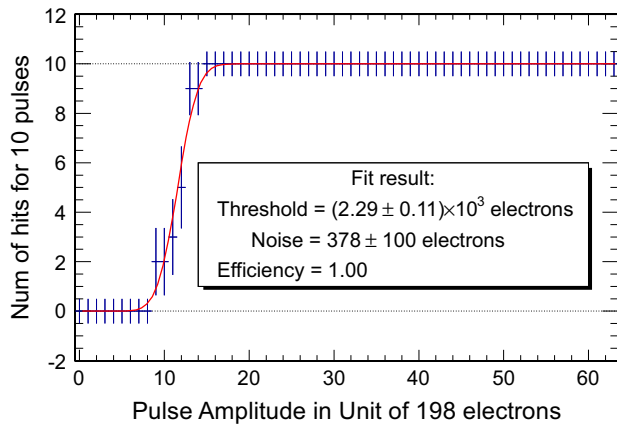


Fig. 35. Typical calibration data for a single channel (data points), fit with a normal cumulative distribution function.

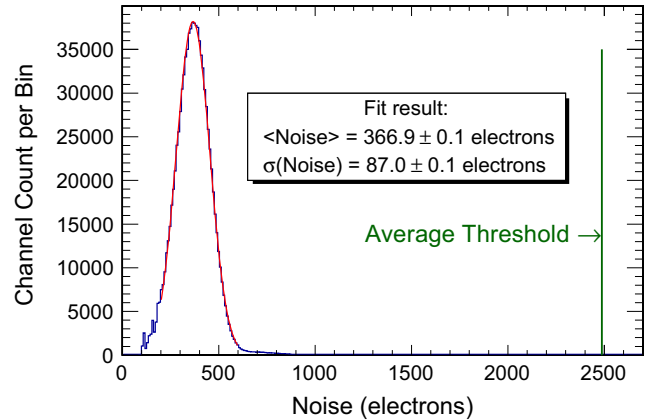


Fig. 36. Histogram of the noise parameter,  $\sigma$ , for all channels under operating conditions, in a typical calibration run. A Gaussian distribution fit to the data gives a mean noise level of 367 electrons. The nominal discriminator threshold at  $\sim 2500$  electrons is shown by the vertical line.

divided into strips with a  $75 \mu\text{m}$  pitch in the radial direction and a  $\phi$  coverage of  $3.75^\circ$ . Groups of custom 128-channel front end read-out ASICs, called FPHX chips, are wire bonded to the sensor.

FVTX sensors display the expected behavior in response to radiation dose. However, measurements of the radiation environment in the PHENIX experimental hall and irradiations of actual FVTX sensors show that radiation effects will not significantly degrade detector performance over the expected lifetime of the experiment.

From data collected at RHIC, the FVTX has demonstrated single particle hit efficiencies above 95%, single hit position resolution better than  $30 \mu\text{m}$ , and electronic noise levels below 500 electrons, all within design specifications.

The data-push architecture of the FPHX read-out chips allows the FEM to receive all hits registered in the silicon sensors without any bias from an external trigger, with minimal processing delay. This feature can potentially allow the FVTX to provide a Level-1 trigger, and can be used to determine the relative luminosity seen by the FVTX detector for each beam crossing. This is useful in polarized  $p+p$  collisions, where the FEM counts all hits, and pairs of coincident hits, above a set ADC threshold for each beam crossing to determine the relative integrated luminosity for each spin orientation. Examinations of these new capabilities and

analysis of data taken with the FVTX in 2012 and 2013 are underway.

## Acknowledgments

We gratefully acknowledge the support of the U.S. Department of Energy through the LANL/LDRD Program for this work. We thank L.J. Bittaker and S. Wender of LANL for assistance with the FVTX sensor irradiations at LANSCE.

## References

- [1] K. Adcox, et al., *Nuclear Physics A* 757 (2005) 184.
- [2] I. Arsene, et al., *Nuclear Physics A* 757 (2005) 1.
- [3] B.B. Back, et al., *Nuclear Physics A* 757 (2005) 28.
- [4] J. Adams, et al., *Nuclear Physics A* 757 (2005) 102.
- [5] C.A. Aidala, S.D. Bass, D. Hasch, G.K. Mallot, *Review of Modern Physics* 85 (2013) 655.
- [6] K. Adcox, et al., *Nuclear Instruments and Methods in Physics Research Section A* 499 (2003) 469.
- [7] A. Adare, et al., *Physical Review C* 86 (2012) 024909.
- [8] A. Adare, et al., arXiv:1310.1005.

- [9] A. Taketani, et al., Nuclear Instruments and Methods in Physics Research Section A 623 (2010) 374.
- [10] J. Hoff, T. Zimmerman, R. Yarema, J. Kapustinsky, M. Brooks, IEEE Nuclear Science Symposium Conference Record (2009) 75.
- [11] J.S. Kapustinsky, Nuclear Instruments and Methods in Physics Research Section A 617 (2010) 546.
- [12] Adhesives Research, ARclad IS-7876 Production Information Data Sheet.
- [13] The 3M Corporation, Novec 7200 Engineered Fluid Technical Data Sheet.
- [14] T. Aaltonen, et al., [arXiv:1301.3180](https://arxiv.org/abs/1301.3180).
- [15] S.N. Ahmed, et al., Nuclear Instruments and Methods in Physics Research Section A 634 (1) (2011) 8.
- [16] F. Hartmann, Nuclear Instruments and Methods in Physics Research Section A 666 (2012) 25.
- [17] P.W. Lisowski, K.F. Schoenberg, Nuclear Instruments and Methods in Physics Research Section A 562 (2) (2006) 910.
- [18] J. Asai, et al., [arXiv:0710.2676](https://arxiv.org/abs/0710.2676).
- [19] G. Casse, et al., IEEE Transactions on Nuclear Science NS-59 (2) (2012) 419.
- [20] H.-J. Ziock, et al., IEEE Transactions on Nuclear Science NS-40 (4) (1993) 344.
- [21] Y. Unno, et al., IEEE Transactions on Nuclear Science NS-42 (4) (1995) 675.
- [22] V. Blobel, Nuclear Instruments and Methods in Physics Research Section A 566 (1) (2006) 5.